MICROSTRUCTURAL AND MECHANICAL CHARACTERIZATION OF DUPLEX STAINLESS STEEL GRADE 2205 JOINED BY HYBRID PLASMA AND GAS METAL ARC WELDING

A THESIS SUBMITTED TO
THE GRADUATE SCHOOL OF NATURAL AND APPLIED SCIENCES
OF
MIDDLE EAST TECHNICAL UNIVERSITY

BY

BURCU TOLUNGÜÇ

IN PARTIAL FULFILLMENT OF THE REQUIREMENTS
FOR
THE DEGREE OF MASTER OF SCIENCE
IN
METALLURGICAL AND MATERIALS ENGINEERING

JANUARY 2012

Approval of the thesis

MICROSTRUCTURAL AND MECHANICAL CHARACTERIZATION OF DUPLEX STAINLESS STEEL GRADE 2205 JOINED BY HYBRID PLASMA AND GAS METAL ARC WELDING

Submitted by **BURCU TOLUNGÜÇ** in partial fulfillment of the requirements for the degree of **Master of Science in Metallurgical and Materials Engineering Department, Middle East Technical University** by

Prof. Dr. Canan Özgen
Dean, Graduate School of **Natural and Applied Sciences** _____

Prof. Dr. Tayfur Öztürk
Head of Department, **Metallurgical and Materials Eng.** _____

Prof. Dr. C. Hakan Gür
Supervisor, **Metallurgical and Materials Eng. Dept., METU** _____

Prof. Dr. Rıza Gürbüz
Co-Supervisor, **Metallurgical and Materials Eng. Dept., METU** _____

Examining Committee Members

Prof. Dr. Tayfur Öztürk
Metallurgical and Materials Eng. Dept., METU _____

Prof. Dr. C. Hakan Gür
Metallurgical and Materials Eng. Dept., METU _____

Prof. Dr. Rıza Gürbüz
Metallurgical and Materials Eng. Dept., METU _____

Prof. Dr. Bilgehan Ögel
Metallurgical and Materials Eng. Dept., METU _____

Assist. Prof. Dr. Kazım Tur
Metallurgical and Materials Eng. Dept., Atılım University _____

DATE: 06/01/2012

I hereby declare that all information in this document has been obtained and presented in accordance with academic rules and ethical conduct. I also declare that, as required by these rules and conduct, I have fully cited and referenced all material and results that are not original to this work.

Name, Last name: Burcu TOLUNGÜÇ

Signature:

ABSTRACT

MICROSTRUCTURAL AND MECHANICAL CHARACTERIZATION OF DUPLEX STAINLESS STEEL GRADE 2205 JOINED BY HYBRID PLASMA AND GAS METAL ARC WELDING

Tolungüç, Burcu

M. Sc., Department of Metallurgical and Materials Engineering
Supervisor: Prof. Dr. C. Hakan Gür
Co-supervisor: Prof. Dr. Rıza Gürbüz

January 2012, 57 Pages

In the present study, the applicability of the hybrid plasma arc welding, in which a keyhole is responsible of deep penetration and a filler wire electrode supplies a high deposition rate, was examined. The microstructural evolutions in grade 2205 duplex stainless steel plates joined by keyhole and melt-in techniques were investigated. The specimens obtained from welded plates having thickness of 8 mm were examined via optical and scanning electron microscopy. Metallographic investigations were supported by X-ray diffraction and energy dispersed spectra analyses by characterizing the phases formed after welding. Impact toughness properties, hardness profiles, and crack propagation behavior of welding zones were quantitatively and qualitatively compared for mechanical characterization. Fracture characteristics were determined via scanning electron microscopy examinations.

It was observed that single-pass HPA weldment seemed to be free of secondary austenite precipitation in acicular form, which is inevitable in multi-pass conventional arc welding methods. Besides δ-ferrite was successfully kept under 70%, which is presented as a limit to not to deteriorate the mechanical properties of DSS. High linear welding speed and high power density supplied by HPAW presented narrower weld metal and heat affected zone with not only lower hardness but also higher impact toughness energies. Synergic effect of the keyhole formed by a plasma arc and the metal transfer supplied by gas metal arc gave reasonable dilution in the weld metal. Furthermore, fatigue crack growth tests revealed that crack propagation rates in HPAW joints were comparable to GMAW joints.

Keywords: Duplex Stainless Steel, Hybrid Plasma Arc Welding, Microstructure, Fatigue crack propagation

ÖZ

HİBRİT PLAZMA VE GAZ METAL ARK KAYNAĞI İLE BİRLEŞTİRMİŞ 2205 DUBLEKS PASLANMAZ ÇELİKLERİNİN MİKROYAPI VE MEKANİK KARAKTERİZASYONU

Tolungüç, Burcu

Yüksek Lisans, Metalurji ve Malzeme Mühendisliği Bölümü
Tez Yöneticisi: Prof. Dr. C. Hakan Gür
Ortak Tez Yöneticisi: Prof. Dr. Rıza Gürbüz

Ocak 2012, 57 Sayfa

Bu çalışmada, hibrit plazma ark kaynağı incelenmiştir. Bu kaynak yöntemi, anahtar deliği tekniği sayesinde derin nüfuziyet ve dolgu teli elektrodu sayesinde ise yüksek kaplama hızına sahiptir. Anahtar deliği ve eritme tekniği ile birleştirilen 2205 sınıfı dubleks paslanmaz (DP) çelik plakalar araştırılmıştır. Kaynaklamış 8mm kalınlığındaki plakalardan elde edilen örnekler optik ve taramalı elektron mikroskobu ile incelenmiştir. Metalografik incelemeler, kaynak işlemi sonrası oluşan ikincil fazların karakterizasyonu için kullanılan X-Işını kırınımı ve enerji dağılımlı X-Işını spektroskopisi yöntemleri ile desteklenmiştir. Kaynak bölgelerinin darbe tokluğu özellikleri, sertlik profilleri ve yorulma çatlak ilerleme davranışları mekanik karakterizasyonu amacıyla karşılaştırılmıştır. Kırılma karakteristikleri taramalı elektron mikroskobu yardımıyla belirlenmiştir.

Tek paso olarak gerçekleştirilen HPA kaynağında, çok pasolu yöntemlerde kaçınılmaz olan ve asikular formda oluşan ikincil östenit oluşumu gözlenmemiştir. Bunun yanı sıra δ-ferrit oranı mekanik özelliklerin bozulması nedeniyle kritik olarak tanımlanan %70'in altında kalmıştır. HPA kaynağı yönteminde elde edilen yüksek kaynak hızı ve güç yoğunluğu, kaynak bölgesinin ve ısıdan etkilenmiş bölgenin dar kalmasına ve bununla beraber düşük sertlik ve yüksek tokluk değerlerine ulaşılmasını sağlamıştır. Plazma arkının oluşturduğu anahtar deliği ve gaz metal arkının oluşturduğu metal transfer etkilerinin birleşimi kaynakta yüksek penetrasyona ulaşılmasına olanak vermiştir. Buna ek olarak, yorulma çatlak ilerlemesi testlerinden elde edilen sonuçlar, HPA kaynaklı örneklerde elde edilen çatlak ilerleme hızlarının, GMA kaynaklı örneklerle karşılaştırılabilir olduğunu göstermiştir.

Anahtar Kelimeler: Dubleks paslanmaz çelikler, Hibrit Plazma Ark Kaynağı, İçyapı, Yorulma çatlak ilerlemesi

To My Beloved Husband

ACKNOWLEDGMENTS

I wish to thank my supervisor Prof. Dr. C. Hakan Gür and co supervisor Prof. Dr. Rıza Gürbüz for their guidance, advice, criticism, encouragements and insight throughout the research.

I would like to express my deepest gratitude to Koray Yurtışık; words are insufficient to describe his contribution both in this thesis and in my life.

Dr. Süha Tirkeş is gratefully and respectfully acknowledged for his efforts and suggestions especially on metallographic evolutions and his support and encouragements throughout the thesis.

I also want to express my appreciation to Göksu Gürer for his efforts, guidance, and helps on mechanical tests and Murat Tolga Ertürk for being there every time I was in need.

I want to thank Sinem Adıgüzel and Esra Çorapçı for their friendship and support and especially their valuable sharing of the good and bad times of the path.

I want to extend my appreciation to my family; my parents Filiz and Metin Anık and my sister Ezgi Anık for their infinite support, my grandmother Semiha Yorgancı for her endless love for education, my aunts Sema Yorgancı and Nur Acardağ for their priceless friendship, my mother and father Gaye and Ahmet Tolungüç for their faith in me, to all my friends and to whomever eased the load on me walking this path.

Finally, I would like to thank my beloved husband for his presence in my life.

TABLE OF CONTENTS

LIST OF TABLES

TABLES

LIST OF FIGURES

FIGURES

CHAPTER 1

INTRODUCTION

Duplex Stainless Steels, DSS; which offer a superior combination of mechanical properties and corrosion resistance due to their balanced content between ferrite and austenite, have been utilized in power reactors, off-shore plants, automotive and (petro) chemical industries. The balanced delta-ferrite, δ, and austenite, γ, content of duplex stainless steel, DSS, offers a good combination of strength and corrosion resistance. Due to its relatively higher strength, DSS has been preferred instead of austenitic stainless steels especially in components like piping and reaction vessels, for which welding is a necessary process in fabrication.

New generation of DSS has good weldability by conventional arc welding methods as long as the heat input and inter-pass temperatures are limited in order to ensure a proper γ to δ ratio in the weld metal and heat affected zone, HAZ [1; 2] DSS solidifies ferritically and than partially transforms to austenite. Moderate cooling rates during welding promote a proper phase proportion. Ferrite is more stable and with the existence of N, CrN and CrN2 precipitate under higher cooling rates [3; 4]. Very slow cooling increases the possibility of the intermetallic precipitations like Sigma and Chi [5]. DSS has a very good stress corrosion cracking, SCC, and intergranular corrosion, IGC, resistance, and strength due to the ferrite content, however ferrite contents in the weld metal and HAZ in excess of 70% resulting in the loss of strength and increased susceptibility to IGC [6].

Key-hole welding allows a capability for deep and narrow weldments and narrow heat affected zone, which minimize residual stresses and distortions of assemblies. Electron beam and laser beam welding methods are utilized without the addition of filler metal. However, autogenous welding of DSS is not preferred since the welds will be very high in ferrite [3; 7; 8]. Such weldments shall be quench-annealed in order to get the correct structure.

In the present study, the microstructural evolutions of 2205 Duplex Stainless Steel joints by varying keyhole conditions were investigated. The specimens obtained from welded 2205 plates having thickness of 11 mm were examined via light optical microscopy and scanning electron microscopy. Metallographies were supported by X-ray diffractions and energy dispersed spectra by characterizing secondary phases formed after welding. Volumetric fractions and the morphologies of ferrite and austenite phases were among the major points to be subjected.

CHAPTER 2

THEORY

2.1. Duplex Stainless Steels

During the last fifty years, duplex stainless steel family has been improved by introducing the nitrogen additions. This was a breakthrough mainly for the weldability of DSS since the use and fields of applications increased [9]. DSS offers an alternative to austenitic stainless steels in many fields of application, such as chemical, oil, and gas industries like pipelines and reaction vessels. The unique combination of two phase structure of δ-ferrite and austenite offers a good combination of strength and corrosion resistance. Ferrite phase introduces strength and local corrosion resistance to the material, where ductility and general corrosion resistance comes from the austenite phase. Therefore, duplex stainless steels have high impact toughness and overall corrosion resistance. Furthermore, their relatively low thermal expansivity makes them useful for shell and tube heat exchangers, and the improved stress corrosion cracking resistance in chloride containing environments of temperatures above 50°C [10].

The ratio of austenite to δ-ferrite is quite critical to preserve the advanced mechanical properties. The duplex microstructure is produced by the adjustment of the δ and γ stabilizing alloying elements [10]. Duplex stainless steels contain high amount of alloying elements which have great effect on mechanical properties. However, high alloy content result in complex phase transformation mechanisms [11]. Decomposition of δ-ferrite and formation of intermetallic phases and precipitates as well as austenite

at between 600 – 1200°C, may cause decrease in toughness and corrosion resistance [12]. The microstructure depends on the alloy composition and thermo-mechanical treatment and to preserve the desired properties, it should be equal mixture of austenite and δ-ferrite.

2.1.1. Physical metallurgy

The importance of alloying elements for DSS was mentioned earlier. Ni, C, and Mn are austenite stabilizers while Cr, Mo, Si, and Nb stabilize δ-ferrite.

Duplex stainless steels can contain high levels of chromium up to 30 wt %. Chromium has a bcc structure below its melting point. It is the main δ-ferrite stabilizer and the other δ-ferrite stabilizer elements are given in the form of a "chromium equivalent" [10].

Nickel has an fcc. structure below its melting point. Nickel stabilizes the austenite phase and duplex stainless steels contain 5 to 9 wt. % of Ni. Austenite stabilizing elements are represented in the form of "nickel equivalent."

Duplex stainless steels contain carbon and nitrogen; both are austenite stabilizers, up to 0.08 and 0.3 wt. % respectively. The addition of C or N increases the maximum solubility of Cr in austenite, which is important for corrosion resistance.

Mo exists in duplex stainless steels in the range of 1 to 3.9 wt. %. After Cr and Ni, Mo is the third important alloying element in duplex stainless steel. Mo is a δ-ferrite stabilizer element and it improves the pitting corrosion resistance.

Another ferrite stabilizer element that exists in DSS is silicon, having an effect similar to that of molybdenum. The addition of 3-5 wt. % Si to duplex stainless steel castings considerably improves the pitting resistance in acidified ferric chloride solution, and at the same time impairs the resistance to intergranular corrosion in boiling nitric acid solution [13].

Other ferrite stabilizer elements are Nb and Ti. Titanium forms TiC precipitates by removing the carbon from the solution, and this may increase the sigma formation since the Cr in the system remains free.

Mn and Cu are mentioned as austenite stabilizing elements. Cu addition improves the corrosion resistance and by precipitation hardening mechanism, it increases the strength of the material. Furthermore, Cu results in fine austenite formation by acting as nucleation site for austenite and pinning the growth of nuclei. Mn increases the solubility of nitrogen in DSS.

Remaining alloying elements in DSS are Pd, Pt, and Ru. Additions of up to 8 wt. % of them to duplex stainless steels promotes an austenitic mode of solidification, reduces martensite formation in the solution treated and deformed materials and accelerates the formation of σ at 900°C on ageing [14].

Duplex stainless steels, apart from some near ferritic alloys with low alloy content, do not undergo a secondary transformation from austenite to ferrite as is usually experienced by low-alloy and carbon steel weld metals. Upon solidification from liquid, δ-ferrite crystallization occurs in 2205 duplex stainless steels. Temperatures around 1200^{o}C, solid phase transformation takes place as the formation of allotriomorphic austenite along the ferrite grain boundaries down to temperatures around 400^{o}C. Further cooling results in the formation of Widmanstatten austenite plates growing into the ferrite grains. Schematic representation of solidification from liquid is given in figure 1.

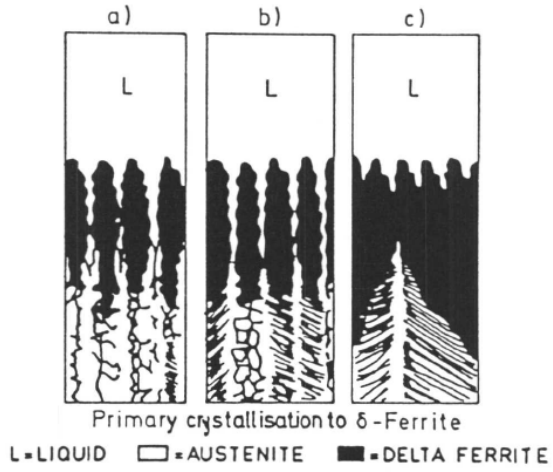

Figure 1: Crystallization modes of duplex stainless steels; ferrite to austenite transformation at high temperatures (a) and (b), complete solidification to ferrite, austenite forms from solid-solid transformation (c) [10].

The solid state transformation is diffusion controlled. The austenite phase is Ni and N enriched whereas Cr and Mo are found in ferrite phase [15]. The nucleation rate of austenite in ferrite is very high. However, transformation could not take place until the sufficient nuclei form at around 1150°C. The relations between the nucleation rate and austenite fraction with temperature are given in Figure 2 (a) and (b) respectively. Ferrite to austenite transformation takes place at temperatures between 600 and 900°C.

Chromium and molybdenum enriched ferrite promotes the formation of intermetallic phases at temperatures around 500-900°C, which are very detrimental to the mechanical properties and the corrosion resistance of the duplex stainless steels [16]. Secondary phases may precipitate at the grain boundaries in the range 450°C-1000°C: they are mainly sigma, chi, secondary austenite, and nitrides (Figure 3).

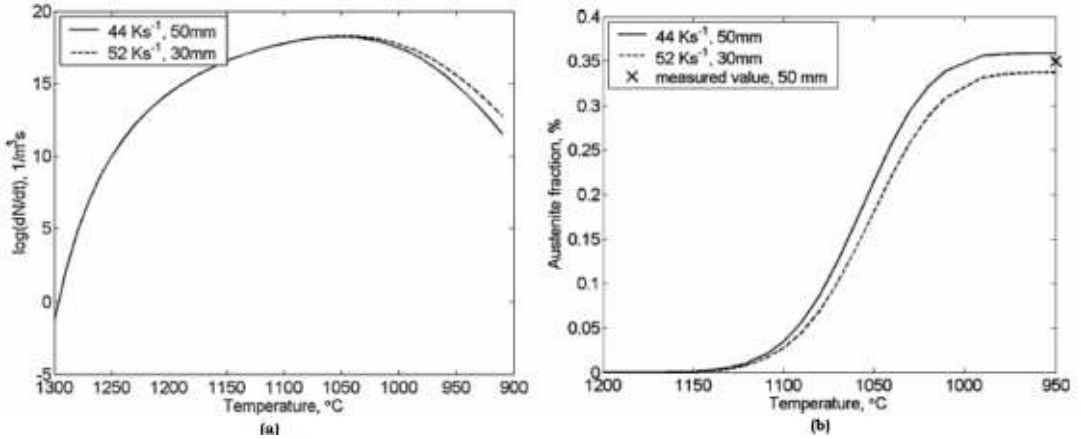

Figure 2: Change in nucleation rate (a) and austenite fraction (b) with temperature [11].

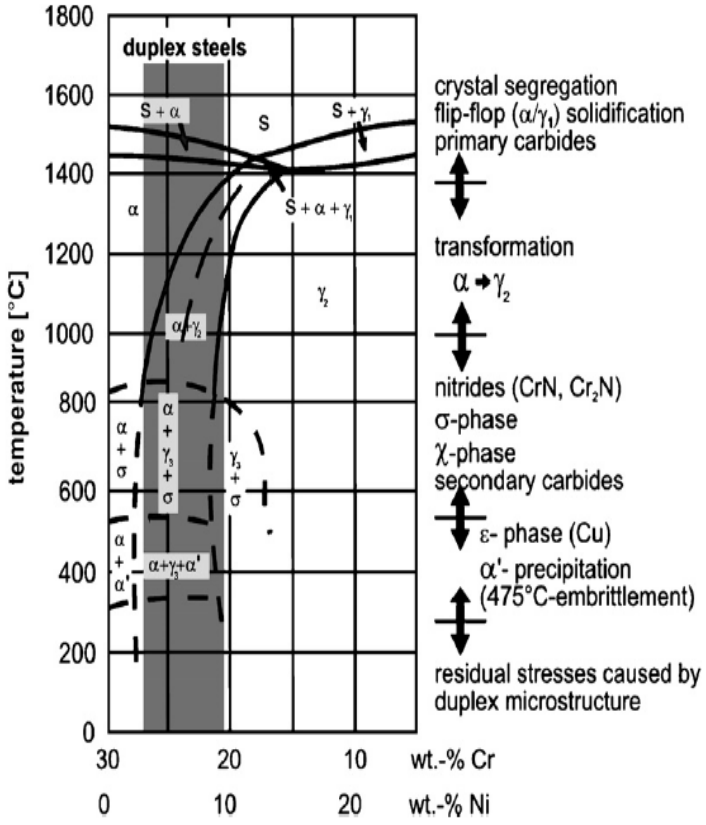

Figure 3: Formation of secondary phases in duplex stainless steels [10].

Table 1 summarizes the crystal structures and chemical compositions of the possible phases could be formed during solidification in DSS. Figure 4

shows the isothermal precipitation diagram for three common types of duplex stainless steels; 2205, 2304 and 2507.

Among those secondary phases, σ is the most important phase because of its significant volume fraction and its strong influence on toughness and corrosion behavior [17]. The formation of sigma phase is associated with a localized depletion of Cr and Mo at grain boundaries. Ferrite grains and δ/δ or δ/γ grain boundaries are prone to the formation of σ phase. Eutectoid reaction of $\delta \rightarrow \sigma + \gamma_2$ creates σ phase after extended ageing times. At the temperature of 900°C and higher, σ phase transformation can occur without austenite formation from δ-ferrite. The compositions of δ-ferrite and sigma phases are very close.

Table 1: Crystal structure and chemical composition of the phases present in DSS [10].

Phase	**Crystal Structure**	**Composition (wt %)**			
		Cr	**Ni**	**Fe**	**Mo**
$Cr_{23}C_6$	fcc	63	5	18	14
Sigma	Tetragonal	29	5	55	11
Chi	bcc	21	5	52	22
R phase	Hexagonal	25.6	-	44.8	27.8
Laves	Hexagonal	11	6	38	45
M_7C_3	Pseudo-hexagonal	$(CrFe)_7C_3$			

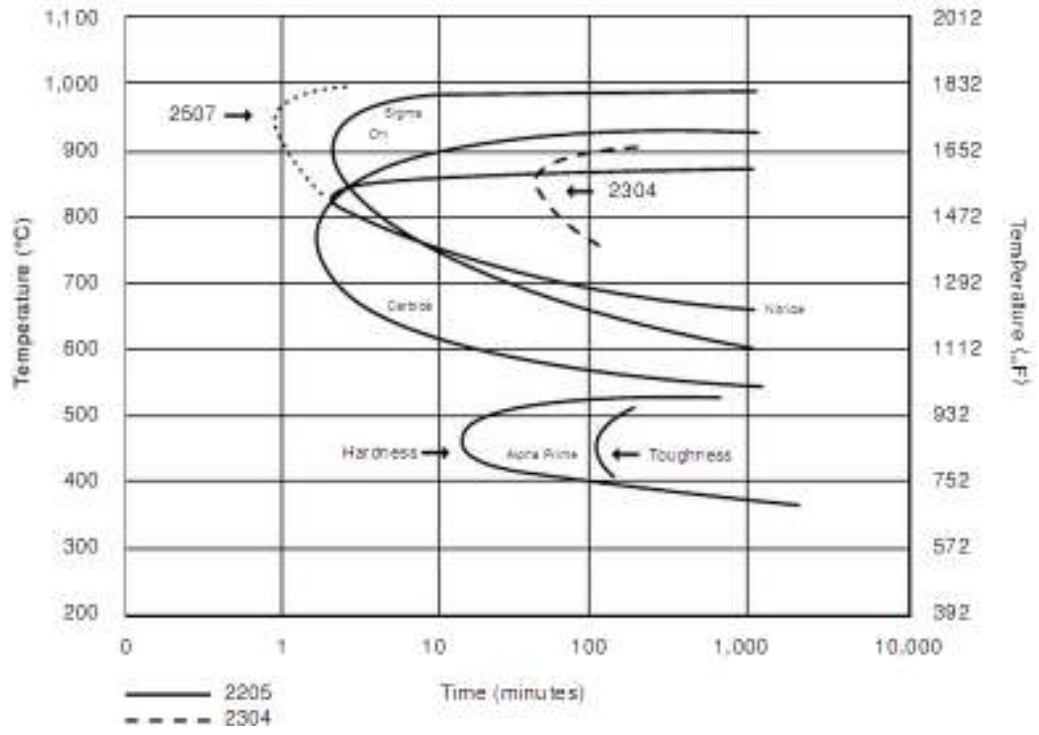

Figure 4: Isothermal Precipitation Diagram for duplex stainless steels, annealed at 1050°C [18].

2.1.2. Mechanical properties

As mentioned before, the mechanical properties of duplex stainless steels are very good especially compared to austenitic stainless steels. The typical mechanical properties are summarized in Table 2.

Table 2: Average mechanical properties of 2205 duplex stainless steels [19].

Tensile Strength (MPa) min	**Yield Strength 0.2% Proof** (MPa) min	**Elongation** (% in 50 mm) min	**Hardness Rockwell C** (HRC)
620	450	25	31 (max)

The yield strength of duplex stainless steels is very high than that of austenitic steels. The high strength introduced by the δ-ferrite phase, yet the strength of DSS is also higher than that of ferritic stainless steels. Therefore, it can be concluded that the duplex microstructure contributes

to the high strength since there exists a mutual hindering of the growth of grains leading to a fine grain structure. Furthermore, nitrogen in austenite gives rise to interstitial solid solution hardening, and this may cause to austenite having a higher strength even than δ-ferrite. The overall high strength of DSS can be linked to the presence of δ-ferrite phase, small grain size, formation of hard secondary austenite, and interstitial and substitutional solution hardening. Away from the microstructural features, cold deformation can improve the yield strength, tensile strength, and hardness of the duplex stainless steels, while it reduces the elongation slightly (Figure 5).

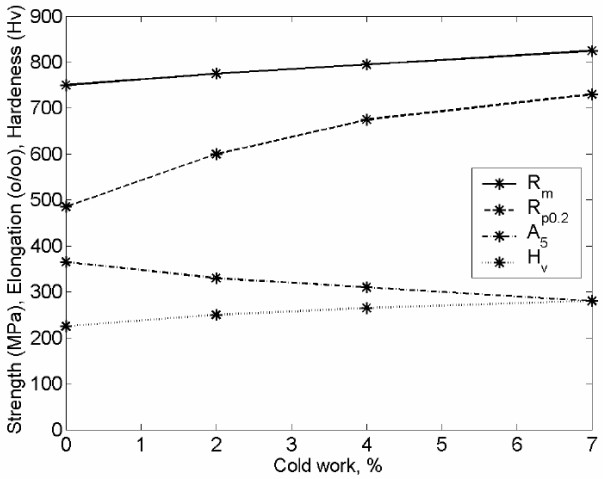

Figure 5: The effect of cold work on the tensile strength (R_m), yield strength ($R_{p0.2}$), elongation (A_5) and hardness (H_V) [20].

Austenite phase introduces high toughness to the duplex stainless steels. However, aging can cause a rapid decrease at around 600-950°C due to the formation of brittle intermetallics [21].

Duplex stainless steels have excellent general corrosion resistance in most environments. Resistance to localized corrosion arises from the ferrite phase while the austenite phase introduces a general corrosion resistance. Two phase microstructure reduces the risk of intergranular corrosion attack caused by Cr depletion. Therefore, in chloride containing environments, DSS are not prone to stress corrosion cracking. Critical pitting temperature

(CPT) of 2205 duplex stainless steel is around 35°C. Grade 2205 will often perform well in environments which cause premature failure of austenitic stainless steels and have better resistance to sea water.

The fatigue strength of DSS corresponds approximately to the proof stress of the material. Aging has a considerable effect on the crack growth rate of duplex stainless steels [20]. Ferrite becomes very hard and only austenite deforms plastically, while local brittle fracture occurs in ferrite. Increasing the nitrogen content promotes the low cycle fatigue resistance by increasing austenite formation [22].

2.1.3. Standards and codes defining Gr 2205

DSS are defined in both European and American codes and standards. EN code of the grade 2205 is 1.4410, and it is 32205 by unified numbering system, UNS.

DSS Gr 2205 plates, sheets and strips are designated as X2CrNiMoN22-5-3 as per EN 10088-2 [23], whereas seamless tubes and pipes made of the material are designated in a same way according to EN 10216-5 [24]. Seamless and welded tubes and pipes of Gr 2205 are standardized in codes ASTM A789 [25] and A790 [26], respectively. While ASTM A182 [27] describes piping fittings made of stainless steels including Gr 2205, ASTM A240 [19] defines plates, sheets and strips of the grade.

The material is approved by the American Society of Mechanical Engineers, ASME, for use in accordance with ASME Boiler and Pressure Vessel Code, section VIII, div. 1 and ASME B31.3 Chemical Plant and Petroleum Refinery Piping. It is approved by ISO 15156-3/NACE MR 0175, Sulphide stress cracking resistant material for oil field equipment, VdTÜV-Werkstoffblatt 508 and NGS 1609 Nordic rules.

2.2. Service Environment of Reaction Vessels

2.2.1. Definition, geometry, and manufacturing

Pressure vessels are used to store fluids under relatively high pressures. Pressure Equipment Directive, PED, defines pressure vessels, in where the pressure is above 0.5 atm [28].

Concerning stress and strain conditions, a sphere is the best shape for a pressure vessel. However, this geometry is expensive to manufacture therefore a common design including a cylindrical body and two heads, which are typically either flat or semi-elliptical or hemi/tori-spherical, has been usually employed for oil, (petro) chemical, nuclear, and mining industries.

2.2.2. Stress and strain

If ratio of the inside radius to the wall thickness of the vessel is greater than 10, than the vessel is classified as thin-walled pressure vessel, which can be considered under shell structures.

An enclosed fluid applies pressure to the shell uniform in magnitude. If the pressure is more or less than the ambient pressure, some stresses and consequently strains will evolve on the wall of the vessel. Stresses are due to the resultant force, F, which is a product of the pressure, P, and internal cross-sectional area of the shell; for cylindrical bodies the cross-sectional area corresponds to πr^2, where r is the radius of the cylinder.

$$F = P\,\pi r^2 \tag{1}$$

Because the pressure and the vessel wall are symmetrical about the axis shown in figure 5 (a), a circumferentially uniform longitudinal stress, σ_l, is produced in the wall. For thin-walled pressure vessels, this stress can also be assumed to be uniformly distributed across the wall thickness, t.

$$F = \sigma_l\, 2\pi r t \tag{2}$$

$$\sigma_l \, 2\pi rt \, = P \, \pi r^2 \tag{3}$$

Consequently, the longitudinal stress produced in the wall can be defined as:

$$\sigma_l \, = \frac{Pr}{2t} \tag{4}$$

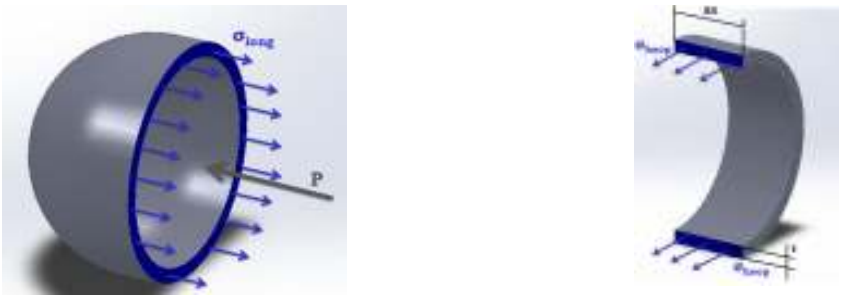

(a) **(b)**

Figure 6: (a) Longitudinal and (b) hoop stresses produced in the wall of a thin-walled pressure vessel.

In order to define the stresses produced in the circumferential direction of the cylindrical shell, the free body in figure 6 (b) can be considered. The net pressure of the fluid acts on the free body will be in lateral direction as shown in this figure. Corresponding force, F, applied to the free body can be formulated as follows:

$$F = P \, 2r\Delta x \tag{5}$$

where Δx is the unit width of the segment chosen on the free body.

This force produces normal stresses, σ_h, in the circumferential direction by the equilibrium equation:

$$F = \sigma_h \, 2t\Delta x \tag{6}$$

and combination of the equation (5) and (6) gives;

$$\sigma_h \, 2t\Delta x = P \, 2r\Delta x \tag{7}$$

$$\sigma_h \, = \frac{Pr}{t} \tag{8}$$

Therefore, the outer shell of the thin-walled cylindrical pressure vessel is subjected to biaxial stress condition composed of a hoop, σ_h , and a longitudinal, σ_l , stress, which gives a plane stress situation for the outer face of the shell (Figure 7).

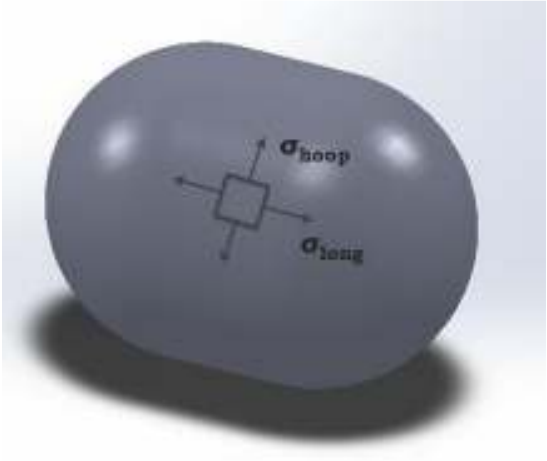

Figure 7: Plane stress situation for the outer shell of the thin-walled pressure vessel.

Generalized Hooke's Law gives normal strains on the outer shell in the longitudinal, ε_l, circumferential, ε_h, and radial, ε_r, directions are as follows:

$$\varepsilon_l = \frac{\sigma_l - \nu\sigma_h}{E} \tag{9}$$

$$\varepsilon_h = \frac{\sigma_h - \nu\sigma_l}{E} \tag{10}$$

$$\varepsilon_r = \frac{-\nu(\sigma_l + \sigma_h)}{E} \tag{11}$$

Since there is pressure of the liquid acting to the inner shell, there will be a triaxial stress condition on the inner surface of the wall, in which a radial stress, σ_r, also contributes. Then the strains become:

$$\varepsilon_l = \frac{[\sigma_l - \nu(\sigma_h + \sigma_r)]}{E} \tag{12}$$

$$\varepsilon_h = \frac{[\sigma_{hl} - \nu(\sigma_l + \sigma_r)]}{E} \tag{13}$$

$$\varepsilon_r = \frac{[\sigma_r - \nu(\sigma_{lh} + \sigma_{hr})]}{E} \tag{14}$$

For a vessel having 1000 liters of volume, 10 mm of shell thickness and working under 50 bars with 2:1 semi-elliptical domed end caps, longitudinal and hoop stresses evolved in the shell might reach about to 100 and 200 Nmm^{-2}, respectively, which corresponds approximately to a forth of ultimate tensile strength of the grade 2205. Corrosive environment and service temperature are also taken into the consideration of shell thickness.

2.2.3. Stresses on longitudinal and circumferential joints

As explained in previous sub-section, hoop stresses are twice as large as the longitudinal stresses introduced in the shell of thin-walled cylindrical pressure vessels.

Due to the internal pressure acting on the inner shell of the vessel, there is an additional stress called radial stress, which is equal to the absolute amplitude of the pressure:

$$\sigma_r = -P \tag{15}$$

Cylindrical pressure vessels generally are manufactured by circumferential and longitudinal welded joints from plates mechanically shaped as cylinders and cones as represented in Figure 8. These joints are subjected to longitudinal and hoop stresses at the weld cap (outer-shell) side, longitudinal, hoop and radial stresses at the weld root (inner-shell) side. Hoop stresses are two times higher in amplitude than longitudinal stresses, therefore longitudinal joints are considered to be more critical in pressure vessel manufacturing (Figure 9).

Figure 8: A typical pressure vessel while being manufactured; (a) longitudinal and (b) circumferential joints (GAMA Industrial Plants Manufacturing and Erection, Inc.).

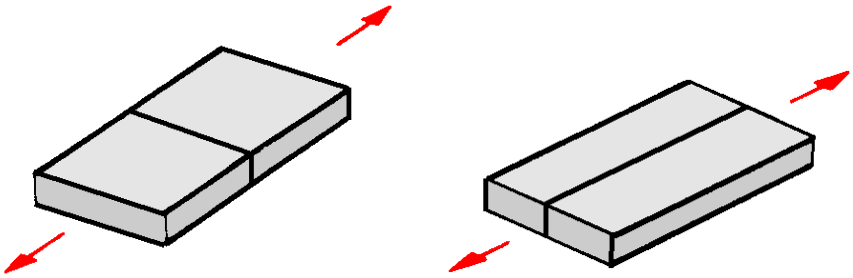

Figure 9: (a) Welding cross-section is totally subjected to the force applied, (b) base material primarily sustains the applied force.

2.2.4. Leak before burst

The term is used to describe a condition for a pressure vessel designed such that a crack on the shell of the vessel will propagate through the wall, which lets the contained fluid out and consequently reduces the pressure before a catastrophic fracture. A reduce in the internal pressure is a valuable hint to

understand that there is a source of leak like cracks. Once it is understood, it is possible to detect the place of the crack by non-destructive inspection techniques.

Generally, pressure vessels are designed for pressure loading of non-cyclic nature. Design By Formulae section of EN 13445-3 [29] provides satisfactory designs when the number of pressure cycles is less than 500 with the safety factor 4 on the ultimate tensile strength, whereas ASME Code [30] takes 1000 with the safety factor of 2.4. As compared with structures subjected to cycling loading like steel or aluminum constructional members, cranes, vehicle components et cetera, fatigue failures are comparatively rare in pressure vessels. However, the avoidance of fatigue is still an important design criterion and the fatigue design rules occupy a considerable per cent of EN 13445-3 [29].

2.2.5. Crack propagation in weldments

In weldments, crack initiation can be suppressed by controlling the microstructure of weld metal and HAZ ensuring that the fracture toughness is sufficiently high for the stress levels to be experienced. However all welding joints consist some discontinuities and a linear discontinuity may be above the critical size for crack initiation. Therefore predicting crack propagation kinetics becomes important not only for the components that are working under considerable cycling stress amplitudes, but also for pressure vessels. Certain mechanical and thermal stresses are introduced to a vessel during system start-up, shutdown, and other changes in the working condition.

The fatigue strength of weldments is primarily governed by their physical profile. Fracture mechanics model and an experimental approach was used to investigate the effect of plate thickness on the fatigue strength of transverse fillet welds in axial loading [31]. Meanwhile, some researchers used a linear elastic fracture mechanics (LEFM) model to predict the fatigue life of the T joint [32]. Concerning full penetration butt (groove) welds where the reinforcement and excess root have been removed, discontinuities in

weld metal and partially melted zone (fusion line) become effective in predicting the fatigue behavior. Linear discontinuities like slag inclusions, gas pores and lack of penetration are common in weld joints. Tips of such linear discontinuities are stress concentrators, which becomes preferable crack initiation sites, with subsequent crack propagation causing structural failure.

Moreover, owing to incompatible thermal strains caused by heating and cooling cycles while welding, weldments contain residual stresses up to yield strength in magnitude. Residual stresses act as a mean stress and reduce the fatigue strength of the joint. The LEFM fatigue life prediction analysis was modified based on an effective stress range and, in doing so, was able to model the residual-stress effect on short-crack growth in as-welded cruciform joints [33].

2.3. Weldability of Duplex Stainless Steels

DSS, combining useful properties of both ferritic and austenitic stainless steels, have been preferred in many engineering applications. DSSs are fusion weldable however; their corrosion resistance and mechanical properties should be adjusted by proper welding parameters that give almost equal phase balance in between austenite and δ-ferrite. Studies has represented that DSS weldments have optimum corrosion and mechanical properties when 35 to 60 % δ-ferrite is maintained. If the δ-ferrite content exceeds 60%, the pitting resistance and ductility considerably decreases. On the other hand, if the δ-ferrite content stays below 35% than it means te solidification mode has changed and detrimental precipitates have formed, which reduces stress corrosion cracking resistance and impact toughness. An imbalance phase distribution may also cause worse fracture toughness and fatigue properties, which are originally other advantages of DSS.

Cooling rate is one of the most important affecting factors for as-welded microstructure of DSSs, which has upper and lower limits in order to have desired metallurgy. Low cooling rates reveal formation of intermetallic phases, whereas high cooling rates may give δ-ferrite content more than

60%. Cooling rate can be adjusted by welding heat input for a specific composition and thickness of the base metal to be welded.

Heat affected zone, HAZ, of DSS is narrower than austenitic stainless steels. DSS weldments have about 50 μm-wide HAZ, which correspond only a couple of grains. Therefore, it is hard to test the impact toughness properties of DSS HAZ by conventional methods [34].

2.3.1. Conventional arc welding methods

Almost all common arc welding methods can be utilized in welding of DSS. Gas tungsten arc welding, GTAW (TIG, 141), shielded metal arc welding, SMAW (E, 111), submerged arc welding, SAW (UP, 12), gas metal arc welding, GMAW (MAG, 135) and flux cored arc welding, FCAW (MAG, 136) have conventionally been used.

Arc welding is a sort of fusion welding, which is a local casting process with respect to the weld seam. Parts to be welded become dies in this casting project and they are subjected to the temperatures from melting point of the base material to ambient temperature. Thus, the metallurgy of the weldment is different from the base material, and the metallurgy of neighboring zones is modified by the heat of welding.

Figure 10 represents weld metal and heat affected zone microstructures from a super-DSS, 2507 joint by SMAW. δ-ferrite /austenite phase balance in base metal changes in annealed zones by the weld heat input. Besides the partially annealed region of the heat affected zone, HAZ is characterized by significant grain growth compared to the base metal. This portion is heated into the two-phase domain. An amount of original δ-ferrite has transformed to austenite on cooling. On the other hand, the over-heated zone is characterized by a relatively lower amount of austenite compared to the melted and partially annealed zones; consequently, a high level of the δ-ferrite phase was present in this region. In the fusion zone (weld metal), austenite precipitates at the boundaries of δ-ferrite grains (allotriomorphic austenite). It is also possible to see austenite grains in the form of

Widmanstätten plates and acicular precipitates (secondary austenite) within the matrix of δ-ferrite in the multi-pass weldments.

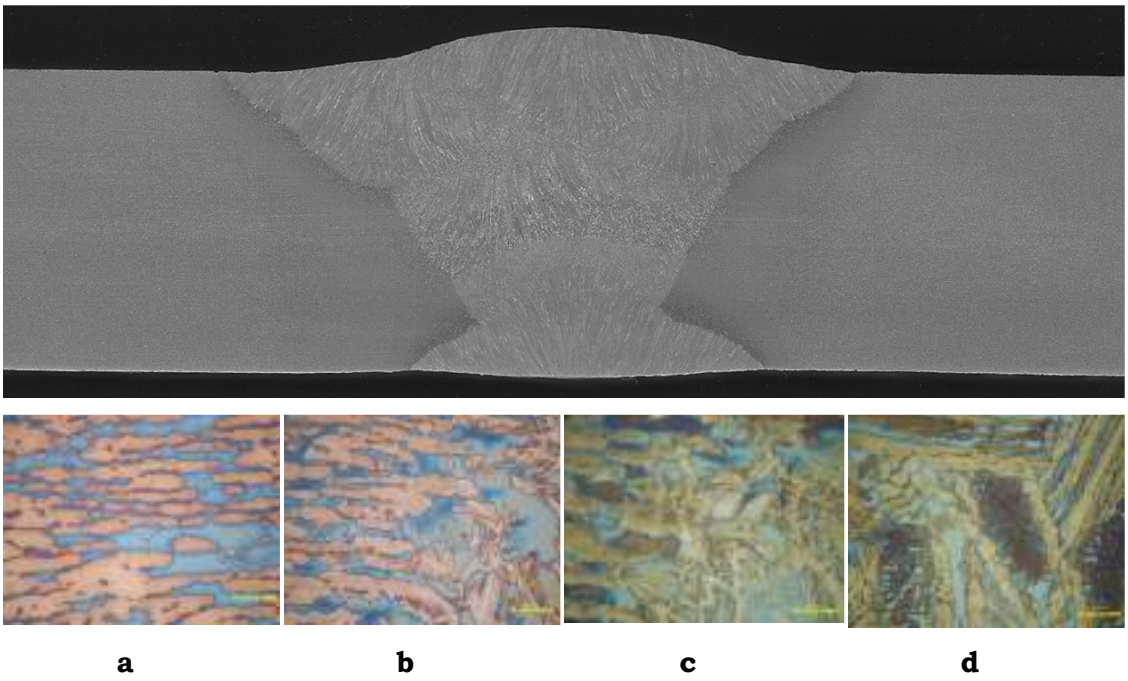

Figure 10: A typical melt-in fusion welded DSS joint; (a) base metal, (b) heat affected zone, (c) fusion line, and (d) weld metal microstructures revealed via Beraha II etchant [35].

Gas-shielded processes give better low-temperature impact toughness in DSS weldments than flux-shielded ones [36]. Although pure Ar is enough to get DSS weldments having good corrosion properties, N are usually added to shielding, N or N and H_2 mixtures can be used as backing gases in order to increase austenite content in the microstructure.

Filler metals consist of extra Ni in order to ensure an appropriate phase balance in the weld metal via promoting transformation from δ-ferrite to austenite and consequently delaying the formation of intermetallics. N additions to filler metals help preventing the precipitating of σ.

Autogenous welding processes are not recommended for DSS, since such processes create welds with very high amount of δ-ferrite [37]. However, a post-weld normalization treatment after autogenous welding processes like laser beam, electron beam and plasma arc welding can be utilized to get

proper phase balance. Besides improvement of hybrid welding techniques of such keyhole processes, in which filler can be added to the weld pool, has started to be applied in DSS welding [38].

2.3.2. Preheating and post weld heat treatment (PWHT)

Depending upon the alloying content, embrittlement may arise at the heat affected zone while welding of steels due to hardening and hydrogen entrapment at relatively fast cooling. In order to avoid embrittlement, the cooling rate must be reduced. Preheating is a way to reduce cooling rates via generating hot spots.

If the expected operating loads make it necessary to reduce residual stresses in welded joints, a post-weld heat treatment, PWHT, is utilized to relieve such stresses. Cold cracking susceptibility due to hydrogen embrittlement is sometimes another reason to perform PWHT for weldments.

Preheating is not recommended for DSS welding because it reduces the cooling rate and may lead formation of undesired phases. Stress relieving post-weld heat treatment processes under AC1 is not applied for DSS because of the risk of intermetallics formation during the treatment. Weldments for sour applications require full solution annealing followed by quenching.

2.3.3. Interpass temperature and heat input

Weld heat input is a major affecting factor for the cooling rate of the weld zones. Higher the heat input, lower the cooling rate, and vice versa. Since there are upper and lower limits for cooling rate for fusion welding of DSS, heat input should also be limited in a range, which is in between 0.5 to 2.5 kJ/mm.

Metallurgical and mechanical properties of weldments are further determined by the cycles of temperature and the duration of welding process besides the heat input. The maximum recommended interpass temperature is in between 180 to 200°C. Exceeding advised interpass temperature limits might cause embrittlement and low impact values for HAZ and lower passes.

2.4. Hybrid Plasma Arc Welding

Hybrid welding is defined by the American Welding Society as the combination two distinct welding energy sources within a single welding process. In fusion welding methods, Hybrid Laser Arc Welding, HLAW, is one of the most popular welding technique, which combines the advantages of a laser beam giving very deep penetration with very low heat input and GMAW giving a considerable deposition rate. Instead of a laser beam, a concentrated plasma arc is preferred for pieces to be welded, where fit-up tolerances are not so tight.

Hybrid Plasma Arc Welding, HPAW, method combines a plasma arc and a gas metal arc into one process. HPAW comprises a sintered tungsten alloy electrode next to a filler wire electrode within a single welding torch. The tungsten electrode is positioned within a fine-bore copper nozzle, in which plasma is forced through. The plasma constricts the arc formed between the non-consumable tungsten electrode and the workpiece by leaving the orifice at high velocities just below the speed of sound. The plasma arc is at the leading position of the welding process, and it creates a keyhole through the thickness of the material. The gas metal arc follows the primary arc and fills the void formed by it (Figure 11).

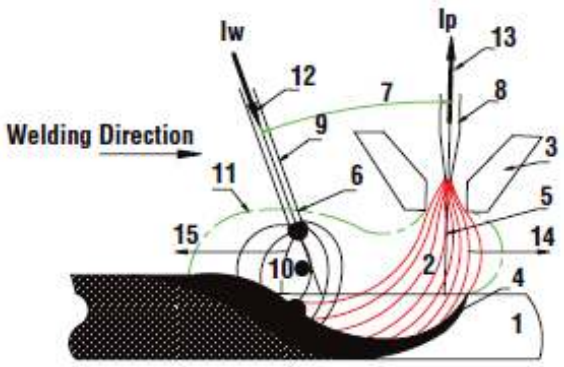

Figure 11: Elements of the HPAW; (1) workpiece; (2) plasma jet; (3) plasma nozzle; (4) melting metal; (5) plasma arc electrode axis; (6) wire axis; (7) angle between electrode's axes; (8) tungsten electrode; (9) consumable electrode (wire); (10) GMAW arc; (11) plasma; (12) wire current (Iw) direction; (13) plasma current (Ip) direction; (14) magnetic forces applied to plasma arc; (15) magnetic forces applied to GMAW arc [39].

The tungsten electrode operates at direct current electrode negative, DCEN, or in other words straight polarity, DCSP, whereas filler wire electrode operates at direct current electrode positive, DCEP, or in other words reverse polarity, DCRP. Two arcs having different polarities apply a magnetic force to each other, which causes a deflection especially of the plasma arc toward the secondary arc. An additional magnetic field is introduced in between two arcs to neutralize this tendency and keep the primary arc toward the front of the weld pool.

2.4.1. Marangoni Effect

The convective flowing of the molten metal from the centre towards the edge is the phenomenon that is called Marangoni-effect. It is working when the gradient of the surface tension of the weld pool is negative [40]. The "reversed Marangoni-effect theory" of HPAW states that the active flux turns the gradient of surface tension of the weld pool from negative (-) to positive (+) which leads to the reversed circulation of the molten metal in the weld pool (Figure 12). The reversed circulation of the weld pool thus keeps towards the centre line and is more intensive. This result finally in deeper penetration compared to conventional welding methods in which the surface tension gradient of the weld pool is from positive (+) to negative (-).

To prove or confute this theory the nitrogen sensitivity of phase balance of duplex would be a very good tool.

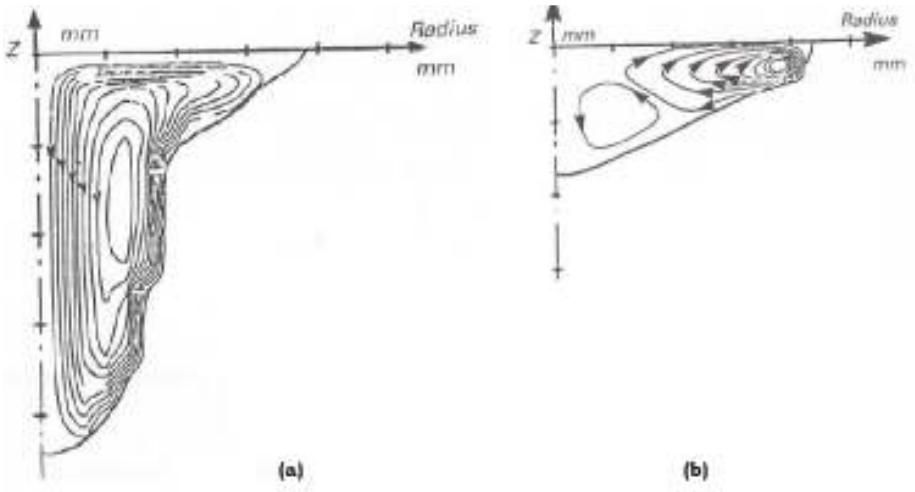

Figure 12: (a) Reversed Marangoni Effect, (b) Marangoni Effect [40].

CHAPTER 3

EXPERIMENTAL STUDIES

3.1. Base Metal Characterization

Standard characterization techniques were used to identify the material received. Duplex stainless steel plates, conforming to ASTM A240 S32205, were obtained and sectioned to the dimensions of 8 mm-thick, 50 mm-wide and 100 mm-long [19]. The chemical constituent of the material was analyzed as per ISO 14284 by spectral analysis [41]. The material was solutionized at 1100°C, and then quenched.

Table 3: Chemical composition requirements for S32205 (2205) in wt % [19].

C	Mn	P	S	Si	Cr	Ni	Mo	N
0.030	2.00	0.030	0.020	1.00	22.0–23.0	4.5–6.5	3.0–3.5	0.14–0.20

For microstructural analysis and hardness measurements, received material was sectioned, grinded on silicon carbide paper mechanically down to 1200 grit, and polished up to ¼ μm with alumina. Electrochemical and color etchants were used to reveal the microstructure. Electrolytic etching was performed with 25 wt% NaOH in aqueous solution for 10 seconds at 4 volts. Beraha's etchant, 10 ml HCl, 100 ml H_2O and 0.5 gram $K_2S_2O_5$, was used in a fresh condition for color etching. Moreover, material was grinded into powder for XRD (X-Ray Diffraction) measurements. X-ray diffractograms were obtained via CuK_α radiation and at 2θ range from 20° to 70° with the scanning rate of 0.5 °/min for phase identification.

For mechanical characterization, micro hardness measurements according to the ASTM E92, with Vickers square-based pyramidal diamond indenter were performed according to the ASTM E92 for each phase. Mechanical requirements of 2205 duplex stainless steel defined by the related standard are given in Table 4.

Table 4: Mechanical test requirements for S32205 (2205) [19].

Tensile Strength (min) MPa	Yield Strength (min) MPa	Elongation (min) %	Hardness (max) HBW
655	450	25	293

Charpy impact toughness tests were conducted for standard characterization, in two dimensions with five specimens for each dimension at -50°C in accordance with EN 100045-1. Standard Charpy impact specimens were prepared with 10x10x55 (mm^3) dimensions and 2 mm V-notches (Figure 13).

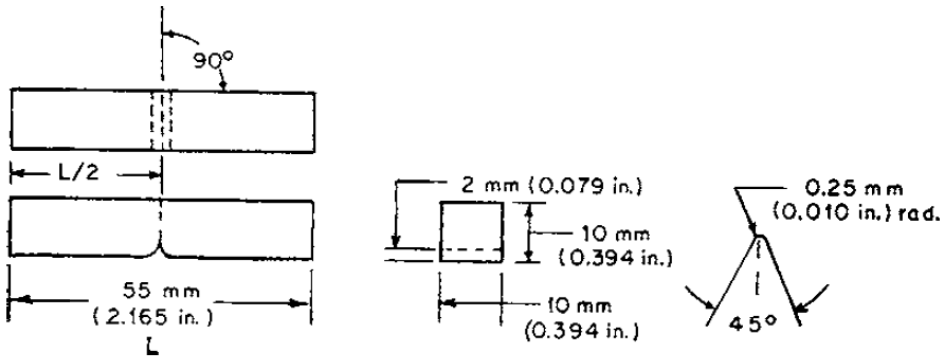

Figure 13: Charpy impact toughness specimen dimensions [42].

Fatigue crack propagation tests were conducted by servo hydraulic machine for comparison the favorable path of crack growth to that of welded joints, according to the ASTM E647. The test was carried out with the same procedure of welded joints which will be explained in section 3.6.

3.2. Welding Parameters

Plates were sectioned to the dimensions of 8 mm-thick, 50 mm-wide and 100 mm-long, and then beveled as per welding technique. Plates were

joined by Hybrid Plasma Arc Welding, HPAW, and Gas Metal Arc Welding, GMAW, techniques at the flat position (1G / PA). The pieces were clamped to a welding platform and the torch was driven by the action of a single-axis translation stage. The contact tube spacing was manually set prior to commencing each weld.

While an arc exists between the filler wire electrode and the workpiece in GMAW, two different arcs exist simultaneously in HPAW; a straight polarity direct current between the workpiece and tungsten electrode and a reversed polarity direct current between the filler wire electrode and the workpiece. A lanthanated tungsten electrode, 2.4 mm in diameter, was used for the HPAW. Weld bevel geometries and welding parameters, subjected to the studies, will be given in chapter 4. Duplex stainless steel solid wire electrodes, 1.2 mm in diameter, conforming to SFA/AWS 5.9 ER2209 and ; ISO 14343 G 22 9 3 NL were utilized in both welding techniques (Table 5). An argon-2% O_2 mixture of gas was used for shielding of the solidifying weld metal and heat affected zone (HAZ) for both techniques. High purity argon (99.999%) was used as orifice gas with the flow rate of 4 lt/min while HPAW performances. The soundness of the resulting test weld joint was confirmed using macro examinations (Figure 14).

Table 5: Chemical composition of the filler wire in wt %.

C	Mn	Si	P	S	N	Cr	Ni	Mo
0.012	1.57	0.42	0.007	0.002	0.15	23.1	8.84	3.21

Heat input comparisons of each welding were carried out. Heat input was calculated from the measured values of arc voltage, current and travel speed. It is simply the ratio of the power to the velocity of the heat source. Heat input is a relative measure of the energy transferred during welding. Equations (16) and (17) show the heat input calculations. During the calculations, basic line energy and heat input definitions were utilized. Heat Input, H (kJ/mm), is a product of Line Energy and Efficiency Factor, η, for a specific welding method, where η is assumed 0.85 for GMAW and 0.5 for HPAW:

$$H = E \times \eta \tag{16}$$

Line Energy, E (kJ/mm), is a product of welding power and linear welding speed, LWS:

$$E = \frac{P(kVA)}{LWS(mm/sec)} \tag{17}$$

Cooling rates were recorded during welding performances by both key hole and GMAW techniques. From 1200°C down to 200°C, the readings were carried out with type-K chromel thermocouples at the center of weld pools with a sensitivity of 41µV/°C.

3.3. Weld Metal Microstructural Characterization

The plates joined using both techniques were sectioned transverse to the weld direction for microstructural characterization. Grinding was carried out with various grades of SiC papers down to 1200 grit followed by polishing using 6, 1, and ¼ µm alumina colloidal. The samples were etched with both Beraha II and Aqua Regia (3ml HCl, 1ml HNO_3) reagents and, electrolytic etching (aqueous 20% NaOH -4 V dc, 10 s). The specimens were examined using light optical microscopy, LOM and scanning electron microscopy, SEM.

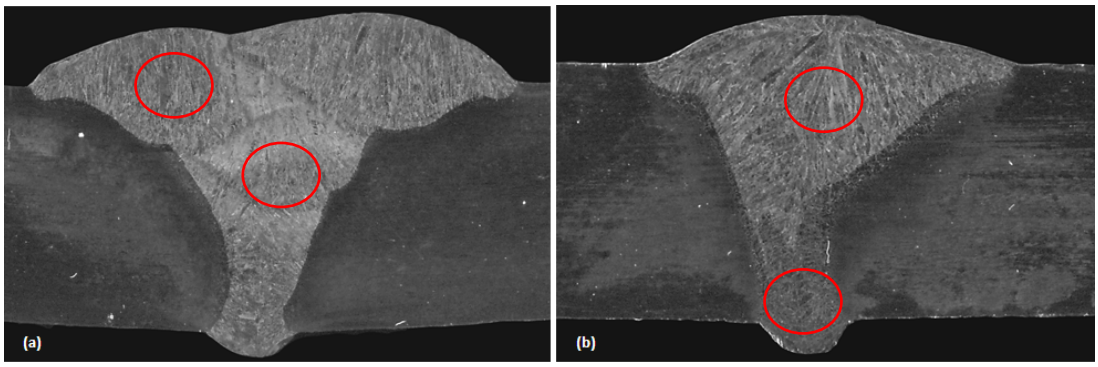

Figure 14: Macro examinations of (a) GMAW, (b) HPAW. The red circles indicate the positions where powders for XRD measurements were prepared.

X-ray diffractograms, obtained via CuKα radiation and at 2θ range from 20° to 70° with the scanning rate of 0.5°/min, were represented in Figure 16 for

different weld and heat affected zones, HAZ, by both technique, and base metal as well.

3.4. Hardness and Charpy Impact Toughness of Weld Metals

The pieces were subjected to Charpy impact toughness tests at -50°C in accordance with EN 100045-1. The Charpy specimens were machined to 10x5x55 (mm^3) with their 2 mm V-notches transverse to the weld direction, perpendicular to the plate surface and centered at the weld metal. Sub-size specimen dimensions and the notch location on welded specimens are given below.

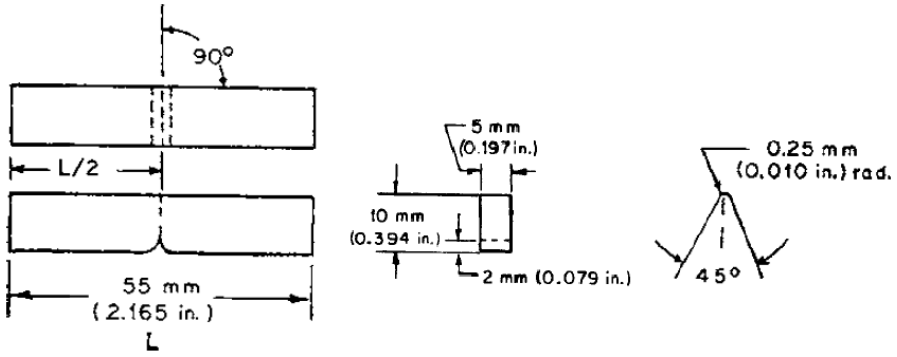

Figure 15: Charpy impact toughness sub-size test specimens [42].

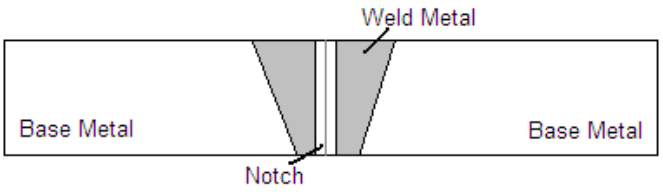

Figure 16: Schematic representation of the notch location on the welded joints.

Microhardness measurements were taken from the welded specimens of both welding method, transverse to the welding direction, 2mm below the cap. Microhardness test equipment was used with a Vickers square-based pyramidal diamond indenter and 4.9N of load. The spacing between the indentations was 0.5mm (Figure 17).

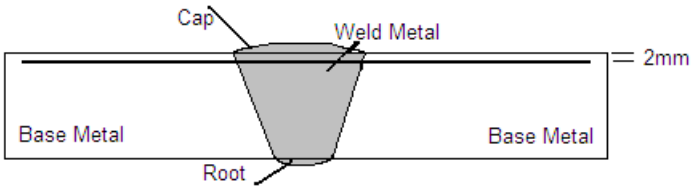

Figure 17: Schematic representation of the indentation locations of hardness measurements.

3.5. Fatigue Crack Propagation Tests

Fatigue crack growth tests were carried out to examine the favorable path of crack growth through the weld metal according to the ASTM E647-11. This test method was chosen for comparison since the weld metal microstructures revealed differences for each joining technique. An MTS servo-hydraulic machine with a capacity of 100 kN equipped with Instron 8500 and controlled by the Fast Track program was utilized. The physical crack length was determined visually by travelling optical microscope with a sensitivity of 0.01 mm.

The testing is based on the hypothesis that it is the stress intensity factor range, (ΔK) that governs the crack rate. The load F varies with constant amplitude between its max and min values. Corresponding stress intensity factors can be calculated and the stress intensity factor range is defined as the difference between them. The crack depth was measured as a function of applied number of cycles. For chosen stages, the crack growth rate, Δa/ΔN, in m/cycle was calculated and plotted against the actual range of the stress intensity factor, ΔK. A schematic representation of crack growth rate vs. stress intensity factor range diagram is given in figure 18. As it can be seen, the crack growth can be divided into three regions; slow crack growth, stable growth and unstable growth. The second stage where the stable crack growth occurs, material constants C and m can be obtained by using Paris-Erdoğan Law.

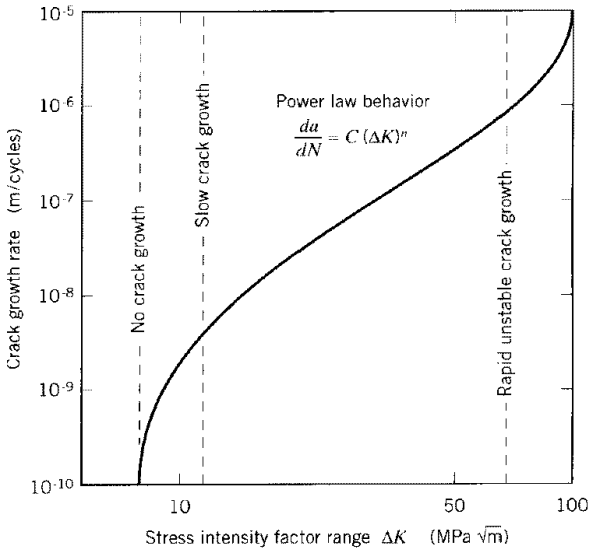

Figure 18: Paris-Erdoğan Law [43].

Compact tension specimens were machined to the dimensions defined in the related standard. Schematic representation of the compact tension specimen is given in Figure 19. Specimens first pre-cracked using K-increasing process under a maximal force of 5500 N and with amplitude of 4050 N. Pre-cracks of 0.95 – 1.20 mm were formed after between 30000 and 40000 cycles. Tests were performed in two orientations; perpendicular to the welding direction and parallel to the welding direction, in longitudinal joints where the stress magnitudes twice more than that observed in circumferential joints under hoop stresses (Figure 20).

Crack lengths were grown to the range of 0.5 - 0.6 W with K-increasing method under a maximal force of 9000 N and with an amplitude of 4050 N (R = 0.10) and a frequency of 20 Hz. Crack-plane orientations were L-T_L and T-L_L (Figure 20).

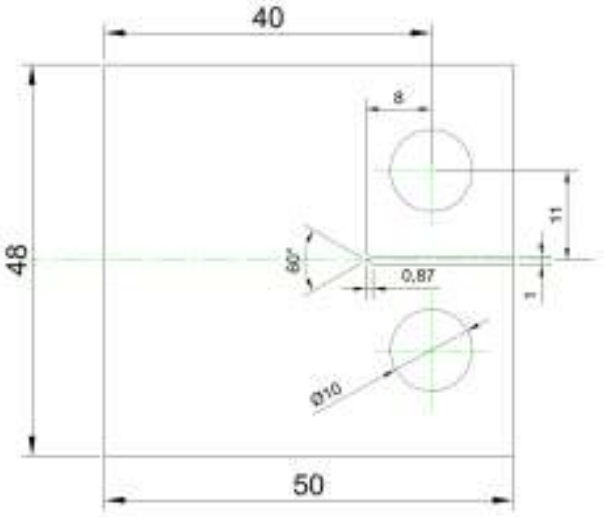

Figure 19: Schematic representation of compact tension specimen for crack propagation tests.

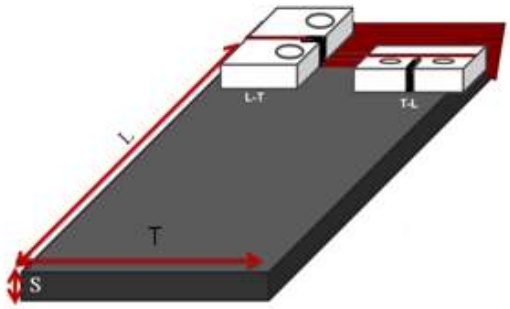

Figure 20: Compact tension specimen orientations on longitudinal joints.

CHAPTER 4

RESULTS AND DISCUSSION

4.1. Base Metal Characterization

Spectral analysis results for base metal can be seen in table 6. The chemical composition of the received material was found to be in the range defined by the related standard, given in figure 21.

Table 6: Chemical composition of the base metal in wt%.

Fe	C	Si	Mn	P	S	Cr	Mo
65.9667	0.0260	0.3903	1.3200	0.0042	0.0050	23.2333	3.0233

Ni	Al	Co	Cu	Nb	Ti	V	W
4.9567	0.2577	0.1367	0.1363	0.0246	0.0113	0.0787	0.2520

Microstructural analysis by LOM and SEM can be seen in figure 21 (a) and (b) respectively. The Beraha II solution was used to etch the sample. Micrographs showed that the structure consists of ferrite matrix and austenite islands. Microstructural analysis was not revealed any sign of intermetallics confirmed by the XRD measurements (Figure 22).

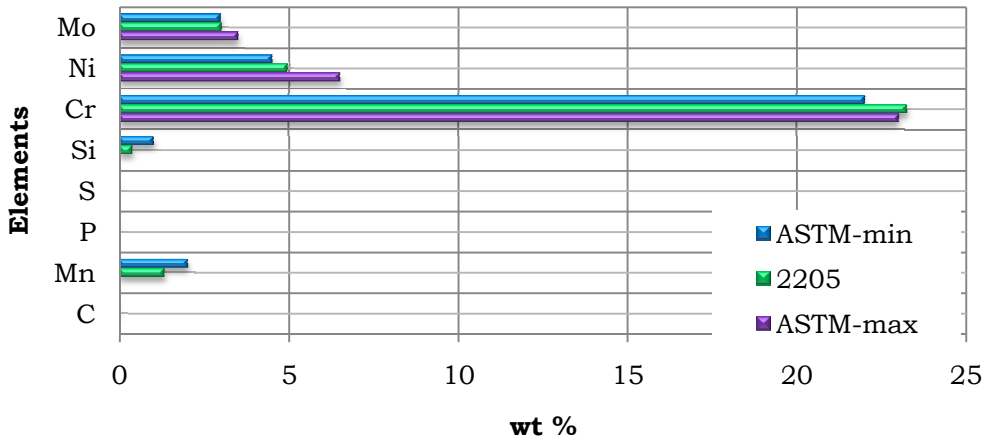

Figure 21: Chemical composition of the base metal compared with the limits defined in ASTM A240.

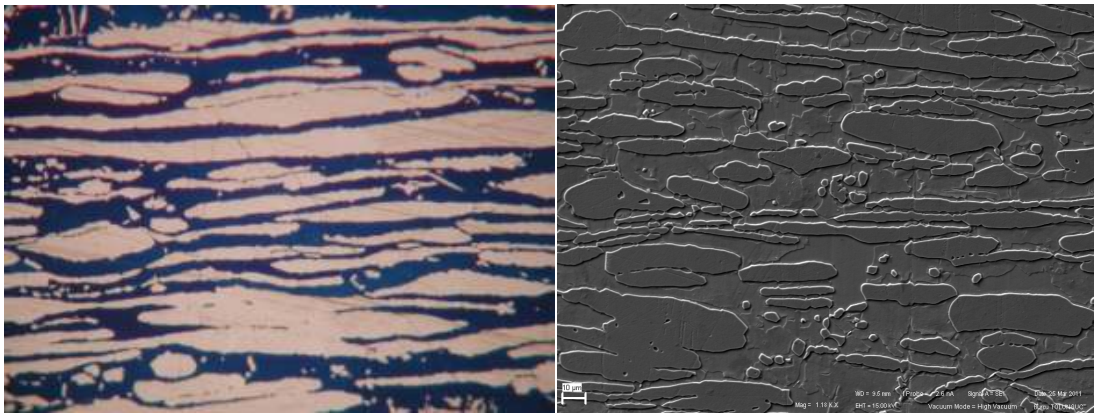

Figure 22: (a) LOM micrograph of the base metal; color etched, (b) SEM micrograph of the base metal.

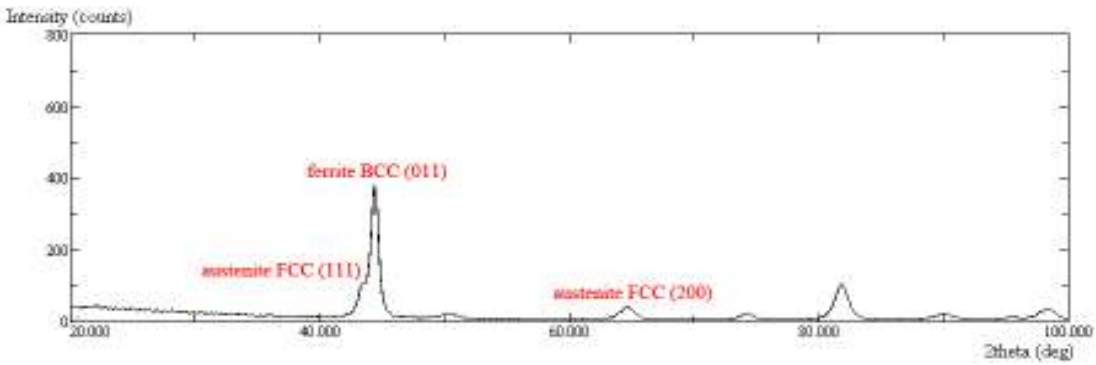

Figure 23: X-Ray diffractogram of the parent metal**.**

Microhardness measurements of the phases and the statistical data are given in Table 7. The hardness of the δ-ferrite phase was found to be higher than that of the austenite as expected. The number of measurements were not enough to make statistical inference, still enough to give an idea. Ferrite came out to be harder than the austenite as expected.

Charpy impact toughness test of the base metal was performed at -50°C with standard size specimens(Table 8). Impact toughness of the base metal came out to be in the range defined by the related standard.

Table 7: Microhardness measurements of each phase present in the base metal.

	1st (HV 0.01)	2nd (HV 0.01)	3rd (HV 0.01)	Hardness (HV 0.01)
Austenite	272	297	294	287.67±11.10
Ferrite	354	368	348	356.67±7.62

Table 8: Charpy impact test results of the base metal

Specimen	Dimensions(mm)	Cv(J)
1	9.7 X 10	220.0
2	9.7 X 9.7	227.0
3	9.8 X 9.8	218.0

4.2. Welding Parameters

Bevel geometry and welding parameters for each technique are given below. For the same plate dimensions, GMAW was performed 4 passes, while the HPA welded only 1 pass.

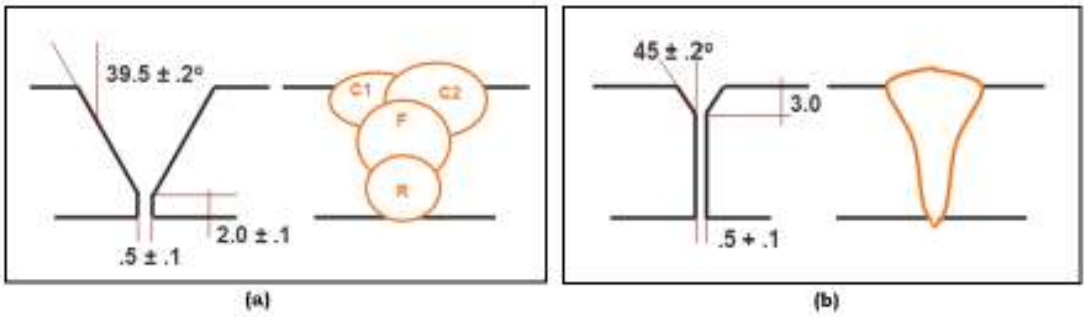

Figure 24: Bevel geometry and schematic representation of passes for (a) GMAW and, (b) HPAW.

Welding parameters are given in Table 9 for both GMAW and HPAW performances where, I_g is gas metal arc current, I_p is plasma arc current, U is arc potential, LWS is linear welding speed.

Table 9: Welding parameters for HPAW and GMAW performances.

	I_g (A)	I_p (A)	U (V)	LWS (cm/min)
GMAW	185-195	NA	24	10.9
HPAW	280-290	180	27	37

Table 10: Comparison of welding consumables for both GMAW and HPAW

	LWS cm/min	T min	MWF g	SGC l	E kWhour
GMAW	10.9	5.01	177	70	50
HPAW	37	1.89	62	117	38

Table 10 summarizes the welding consumables for both techniques; t is the total welding time, MWF is the mass of wire fed, SGC is the shield gas consumption and E is the energy consumed. From the economical point of view, HPAW seems to be advantageous over GMAW.

Heat input calculations for each pass of GMAW, carried out according to the equations (16) and (17) are given in Table 11. Similarly, Table 12 gives the heat input calculation for single pass HPAW.

The keyhole obtained by high-power-density arcs, and laser or electron beams as well, introduces deep penetration with a narrow bead resulting thinner HAZ and less residual stresses due to lower heat input. It was calculated that while HPAW introduced 0.60 kJ/mm, line energy given by a pass of GMAW was 0.61 kJ/mm and total heat input was 2.45 kJ/mm (Tables 11-12).

Table 11: Welding parameters and heat input results for each pass of GMAW.

Passes	W- Current (A)	WFS (m/min)	Voltage (V)	LWS (mm/min)	H (kJ/mm)
Root	185 – 195	8.50	24.0	400	0.61
Fill	185 – 195	8.50	24.0	400	0.61
Cap 1	185 – 195	8.50	24.0	400	0.61
Cap 2	185 – 195	8.50	24.0	400	0.61

Table 12: Welding parameters and heat input results for HPAW.

W-Current (A)	WFS (m/min)	E-Current (A)	Voltage (V)	LWS (mm/min)	H (kJ/mm)
280-290	15.0	180	27.0	800	0.60

Tables 11, 12 show the welding parameters; wire current (W), wire feed speed (WFS), voltage, linear weld speed (LWS) and heat input (H) results for both welding techniques.

Cooling curves for HPAW and GMAW practices from 1200 to 500^{o}C are given in figure 24, where, the measurements for GMAW represents the cap pass. Cooling time measurements for each pass of GMAW were carried out also. $\Delta t_{12/5}$ durations were recorded as 3.33 and 8.82 seconds during the HPAW pass and the GMAW cap pass, respectively.

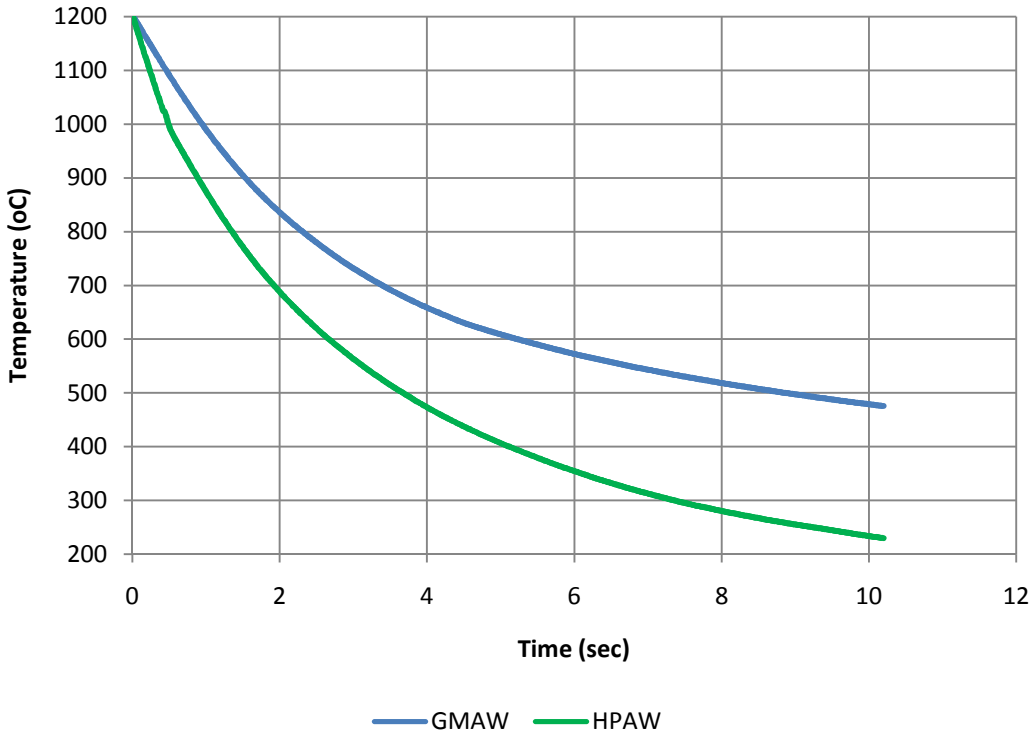

Figure 25: $\Delta t_{12/5}$ durations for GMAW cap pass and HPAW.

During continuous cooling, there is not enough time for the austenite to precipitate until the temperature has decreased to about 1150°C, when a sufficiently amount of nuclei has been formed. Austenite is primarily formed as allotriomorphs at columnar dendrite boundaries below 1150°C by a considerable diffusion rate of austenite former elements. At about 450°C, diffusion slows down in equilibrium conditions and it rises when the cooling rates are higher; $t_{12/5}$ durations can be used to predict the width of allotriomorphic austenites. Higher the $t_{12/5}$, wider the allotriomorhs are expected.

From the experimental data given in figure 25, it can be seen that the cooling time of GMAW ($t_{12/5}$) was around 9 seconds whereas $t_{12/5}$ of HPAW was measured only ~3.5 seconds. Therefore, GMAW performances were expected to form wider allotriomorhs compared to HPAW. Optical microscope studies supported that theory as it can be seen from figure 26.

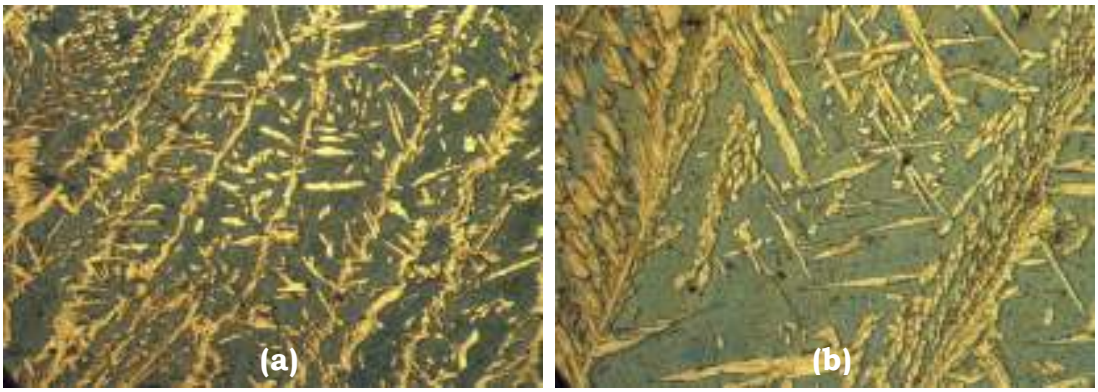

Figure 26: Optical microscope images of (a) HPAW, (b) GMAW-cap pass, showing the allotriomorph widths (X 200).

4.3. Weld Metal Microstructural Characterization

Optical microscope images of the fusion zone for both joining methods are shown in figures 27 and 28. HPA weldments have slightly more δ-ferrite than GMAW cap welds, which is less than 60%. However, phase balance is deteriorated in GMAW fill passes, in which γ occupies more than 70% of the weld metal due to the acicular precipitation. On the other hand, an autogenous zone at the root side of HPA weld metals was observed again deteriorating the phase balance by high amount of δ-ferrite.

As it can be seen from figure 27, especially at the root of weld zone where the examinations revealed that there was no filler penetration, the amount of ferrite phase increased.

Although HPA weld was deposited with an equal heat input for the single pass to that used for each pass in GMA weld, it is seen that the columnar grains in the fusion zone of HPA weld have considerably less coarse grain sizes than GMA welds. Cooling rate is a function of the heat input by the welding process and temperature of the material before welding, factors affecting heat transfer mechanisms as well. Taking the inter-pass temperatures (200°C) into consideration, the specimen joined by GMAW was subjected to 4 heating cycles and kept over 200°C for almost 5 minutes. Moreover, former passes (root and fill) were subjected to the heat treatment by GMAW cap passes, which motivated secondary γ nucleation in ferrite

matrix and precipitation in acicular form (Figure 28 b/d) in the weld metal. However, acicular γ formation could not be observed in HPAW weld metal and GMAW cap passes.

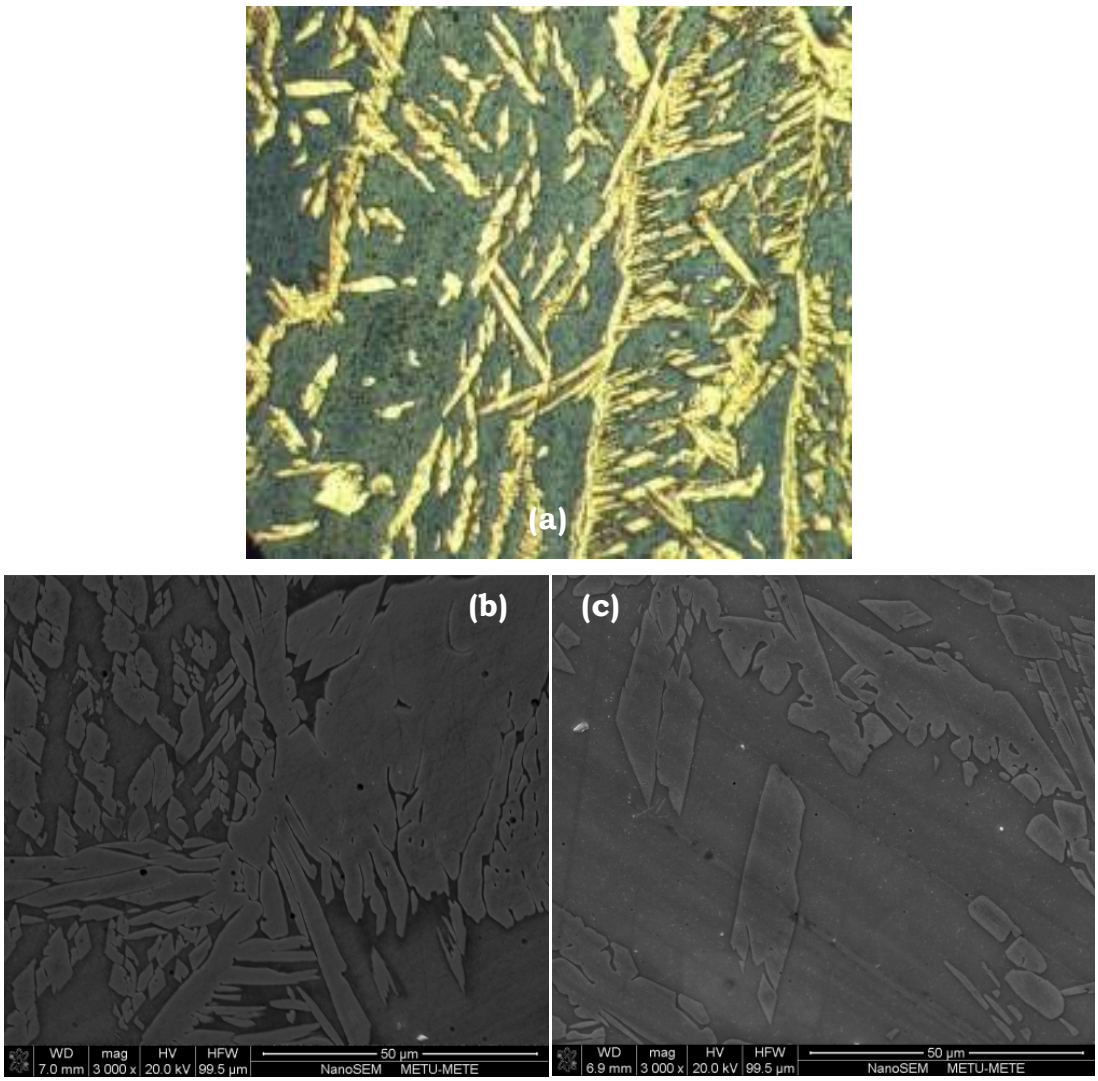

Figure 27: Micrographs of HPA welded specimen; (a) LOM image, X200, (b) SEM image taken from cap side and, (c) SEM image from root side.

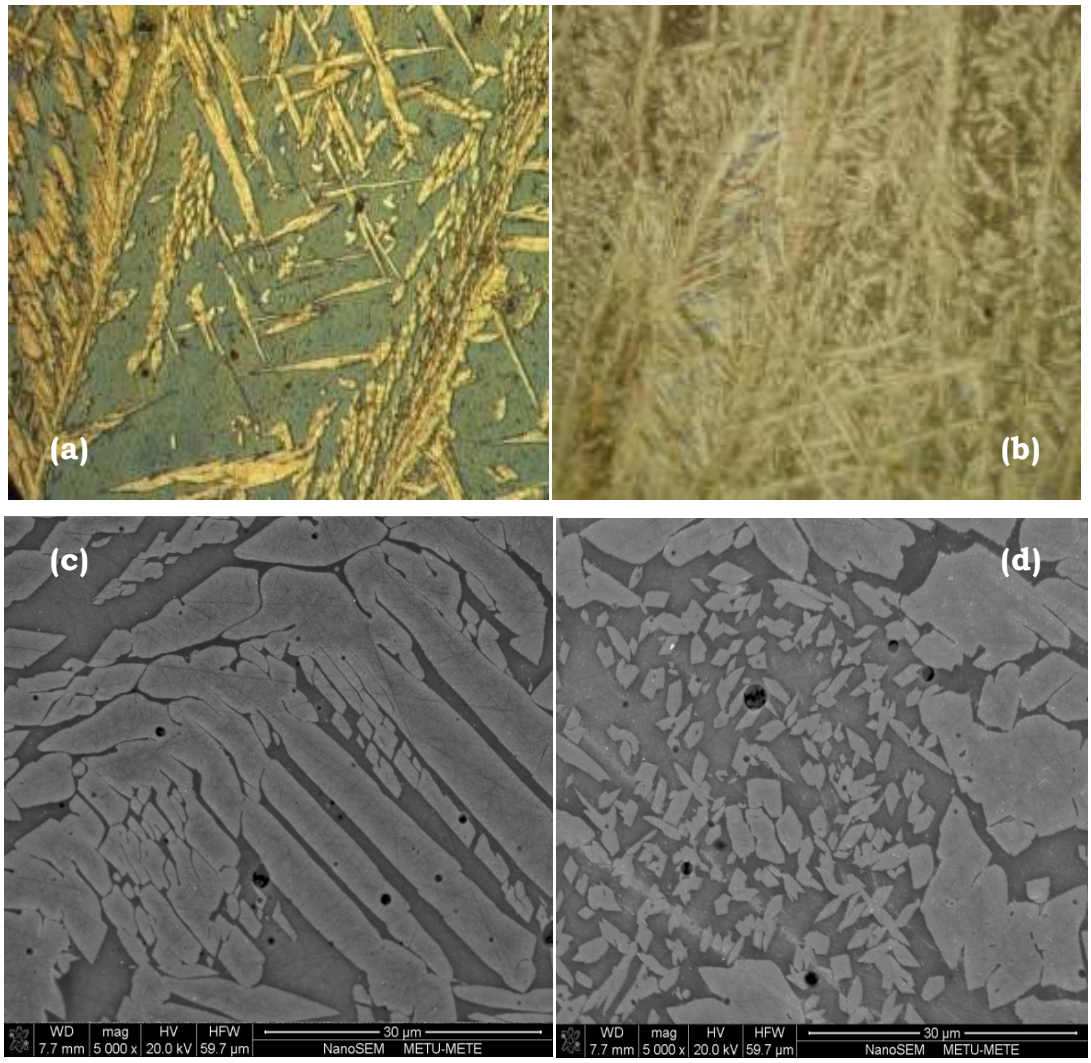

Figure 28: Micrographs of of GMA welded joint; (a/c) cap pass images via LOM and SEM, (b/d) fill pass images via LOM and SEM.

Furthermore, figure 29 shows X-ray diffractograms taken from different zones in both weldments. Powders were obtained from HPAW root zone, HR, HPAW cap zone, HC, GMAW fill pass, GF, and GMAW cap passes, GC.

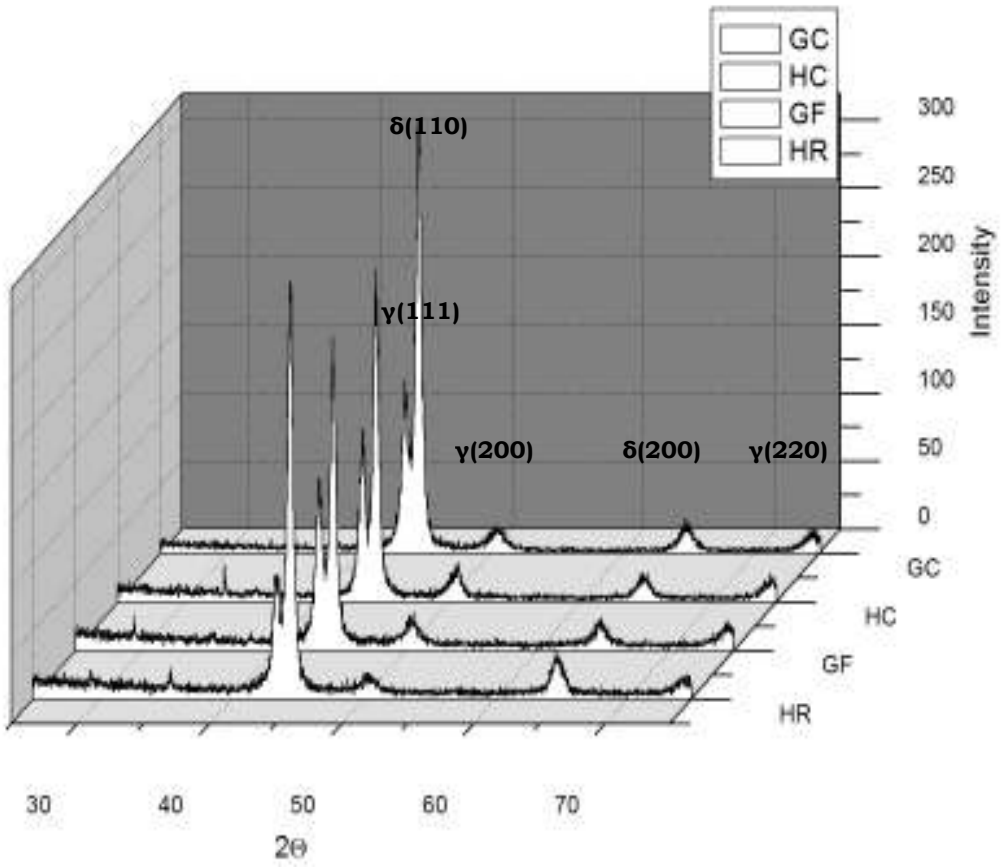

Figure 29: X-ray diffractograms from weld metals of joints by HPAW and GMAW.

4.4. Hardness and Charpy Impact Toughness of Weld Metals

Hardness profiles of each welding technique are given in Figure 30. From the hardness profiles and the macro examinations estimated heat affected zone (HAZ) widths are also given in the mentioned figure. Vicker's hardness profiles from the center of weld metal to the base material in which the profiles reached plateau at less than 4.00 and 7.25 mm for HPAW and GMAW, respectively, indicating approximate widths of HAZ for both welding methods. HAZ dimensions observed were proportional to the cooling rates for one pass of HPAW and four passes of GMAW. Micrographs showing HAZ for both techniques reveal not only thinner HAZ in HPAW joints but also less grain coarsening.

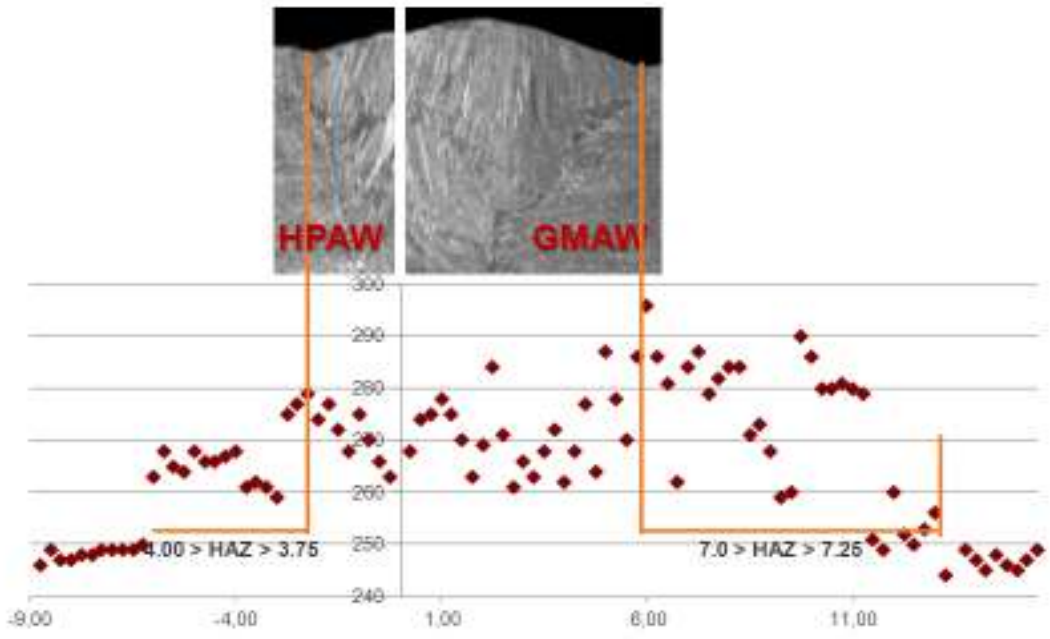

Figure 30: Vickers hardness profiles of the welded specimens and the width of the heat affected zone for each technique.

Charpy impact toughness tests were carried out at -50°C as stated in the related standard. The specimens were machined to the sub-sized specimens according to the standard. The main reason for that the plates to be welded had 8mm thickness. Three specimens for each welding were used and the results of all are given in Table 13.

GMAW seemed to reveal a hard and brittle microstructure than HPAW when the hardness profiles and the Charpy impact toughness results were combined.

Charpy impact fracture surfaces included varying proportion of cleavage and dimple character (Figure 31), while the parent metal specimens provided fracture surfaces had completely a dimple rupture mode of fracture and impact toughness mean energy of 88 J at – 50°C.

Table 13: Charpy impact toughness results for both welding techniques.

Specimen	Dimensions(mm)	Cv(J)
GMAW-1	9.7 X 5	78.0
GMAW-2	9.7 X 4.7	67.0
GMAW-3	9.8 X 4.8	70.0
HPAW-1	9.8 X 4.8	139.0
HPAW-2	9.8 X 4.0	143.0
HPAW-3	10 X 5	145.0

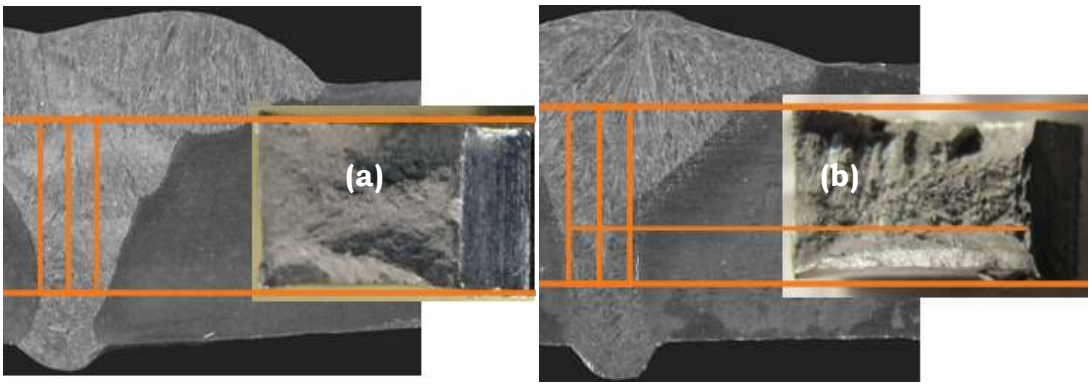

Figure 31: Charpy impact toughness specimens and locations, (a) GMAW and, (b) HPAW.

An analogy between the δ content and the fracture mode was observed on the fracture surfaces of specimens. The specimen obtained from HPA weldments represented a dimple rupture mode of fracture at the upper zone (Figure 32 a), while the mode was cleavage at the root, in which δ dominates due to the autogenous solidification (Figure 32 b).

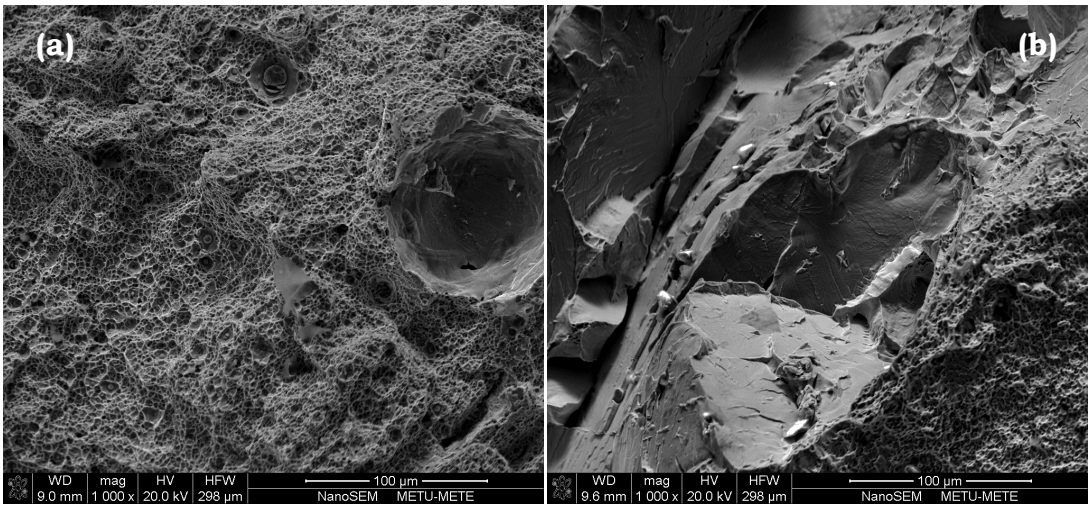

Figure 32: SEM images showing fracture surfaces of Charpy impact test specimens of (a) HPAW upper zone and, (b) HPAW root zone.

4.5. Fatigue Crack Propagation Tests

Results of crack propagation tests carried out in two orientations are given in figures 33 and 34 as crack length (a) versus number of cycles (N) graphs. Test specimens of parent metal, HPA weldment and GMA weldment were presented in the same graph for each orientation in order to ease of comparison.

Crack growth rate versus stress intensity factor graphs are given in Figures 35 and 37 for the two orientations. Crack growth rate data were obtained by calculating the slope of a line passes through two nearest points from a vs. N diagrams. Stress intensity factor range for each crack length was calculated according to the related standard. Equation 20 gives the formula used,

Where; $\alpha = a/W$ when $a/W \geq 0.2$.

$$\Delta K = \frac{\Delta P(2+\alpha)}{B\sqrt{W}(1-\alpha)^{3/2}}(0.886 + 4.64\alpha - 13.32\alpha^2 + 14.72\alpha^3 - 5.6\alpha^4) \quad (20)$$

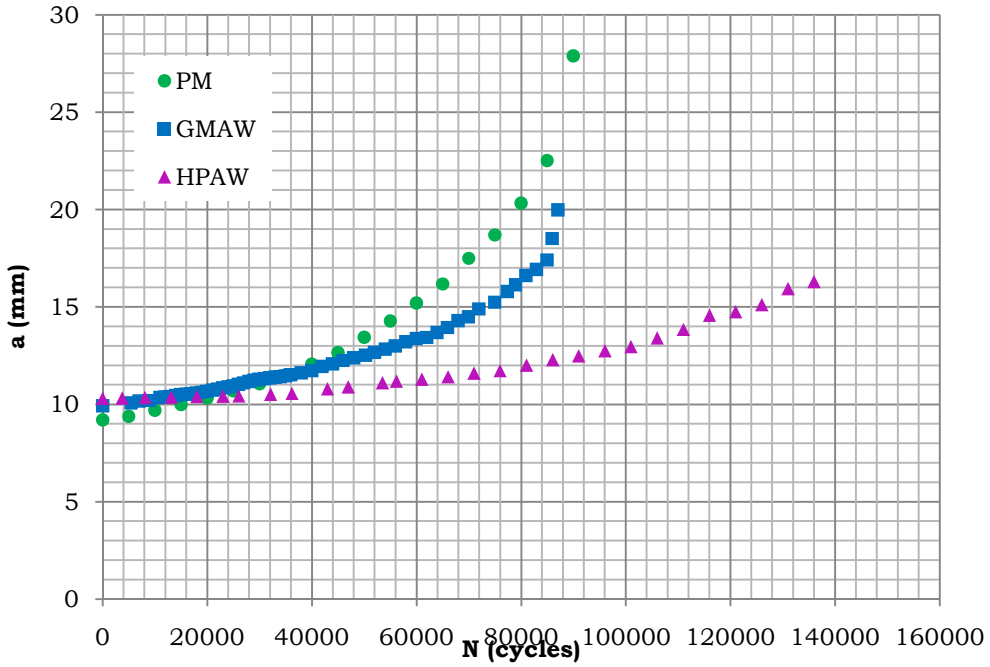

Figure 33: a vs. N diagrams obtained from fatigue crack propagation tests in L-T_L orientation.

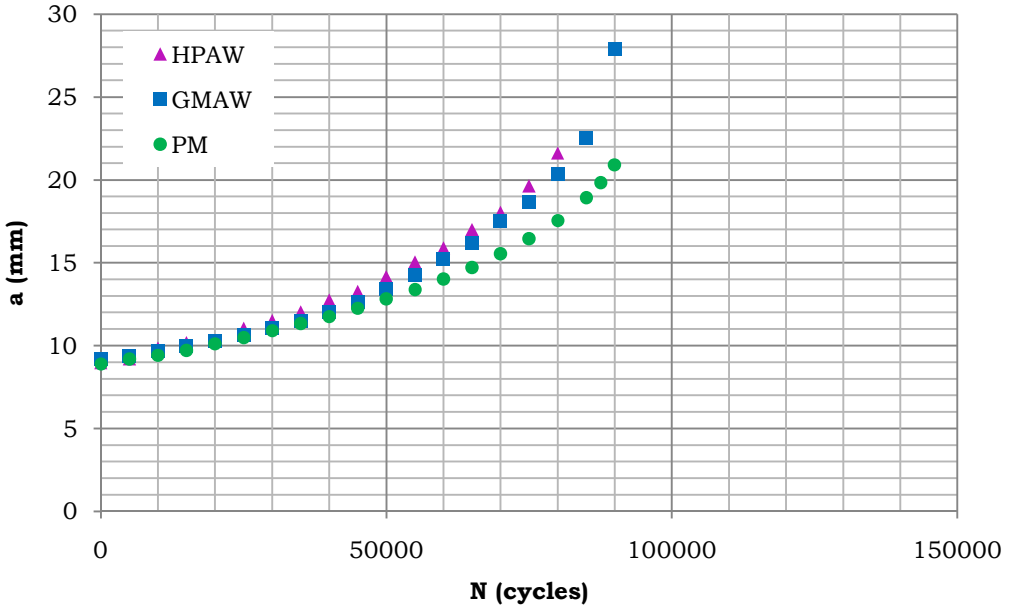

Figure 34: a vs. N diagrams obtained from fatigue crack propagation tests in T-L_L orientation.

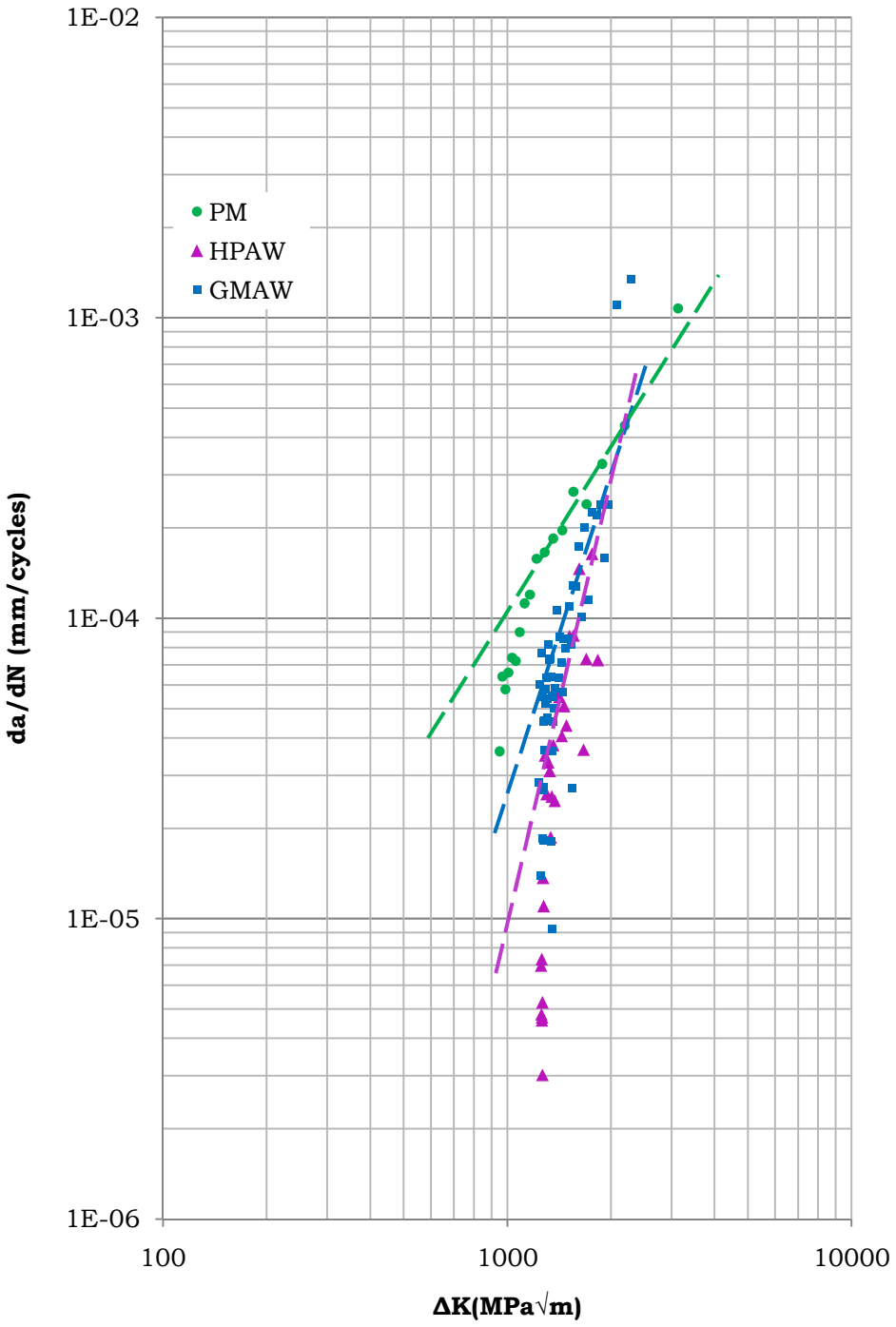

Figure 35: Crack growth rate vs. stress intensity factor range diagram for L-T_L orientation.

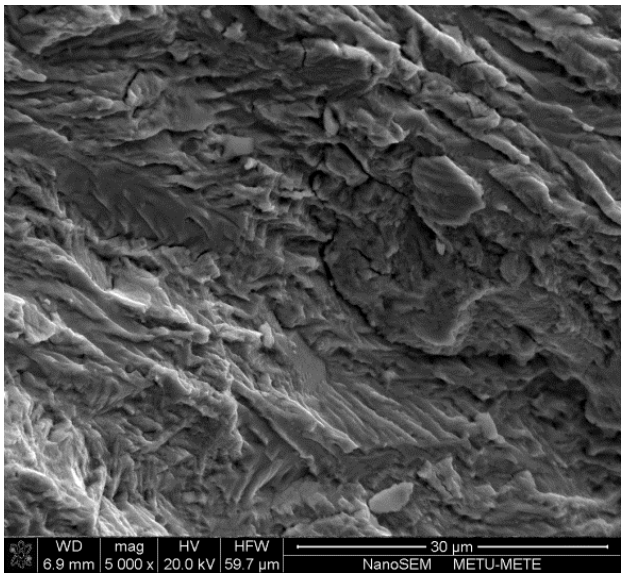

Figure 36: Fracture surface SEM image of HPA welded specimenin L-T_L orientation.

Crack propagation rate in parent metal came out to be higher in T-L orientation compared to that of in L-T orientation. In L-T orientation, when the crack is assumed to propagate in the welding zone and parallel to the welding direction, HPAW had the highest crack growth rate.

Higher δ-ferrite phase amount caused cleavage type of fracture in HPAW (Figure 35). Studies in the literature point out that, as austenite phase fraction increases, the crack growth rate decreases [44]. Therefore, high ferrite phase amount, especially at the root where an autogeneous type of welding observed, should be prevented in HPAW.

When the case where crack assumed to propagate perpendicular to the weld zone, in T-L_L orientation, was examined, GMAW seemed to have a slightly higher crack growth rate. This may be explained by the fact that HPAW reveals a thinner HAZ and fusion zone so that crack mostly propagates in the parent metal. Furthermore, it is known that acicular austenite formation causes grain boundaries to become a favorable path for crack propagation [44]. This may be disadvantage of GMAW where high amount of acicular austenite formation was observed in filler passes combined with coarse grain size.

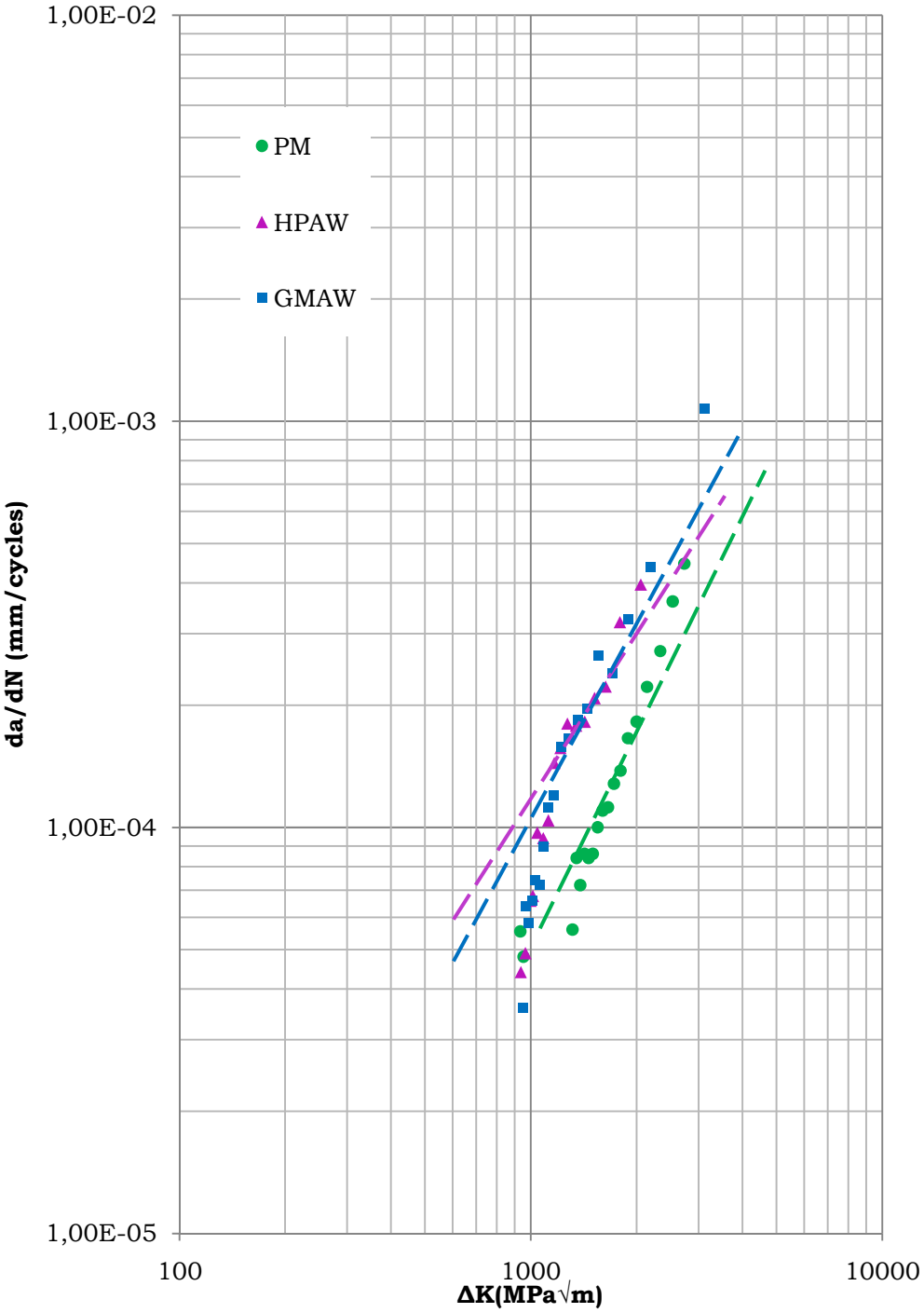

Figure 37: Crack growth rate vs. stress intensity factor range diagram for T-L_L orientation.

Table 14 summarizes the material constants in Paris-Erdoğan Law, obtained by graphically from figures 35 and 37. Paris' Law can be used to

quantify the residual life of a specimen given a particular crack size. Here, m seemed to have a greater influence by being in a power law relationship.

Table 14: Material constants C and m.

		C	m			C	m
L-T	**PM**	$2.96\ 10^{-14}$	2.107	T-L	**PM**	$1.96\ 10^{-15}$	2.286
	HPAW	$2.30\ 10^{-26}$	4.610		**HPAW**	$7.57\ 10^{-15}$	2.229
	GMAW	$2.75\ 10^{-24}$	4.188		**GMAW**	$8.71\ 10^{-17}$	2.644

Fatigue crack growth tests carried out in T-L_L orientation can also be considered as a study of crack propagation in weld zone and HAZ (Figure 38). Therefore, crack growth can be divided into three regions having different slopes. Figures 39 and 40 show the crack propagation and crack length or distance travelled by the crack relation for HPAW and GMAW.

Stage 1 of crack growth, where the crack is very small in size and propagation takes place in very small increments, coincided with the fusion zone of HPAW. Therefore, data taken from there may have included experimental errors. On the other hand, from the data obtained by using Paris-Erdoğan Law in second stage of crack growth, it seemed to have a higher growth rate compared to other regions (Figure 39). Crack growth in the HAZ seemed to start fast and then slow down as it reaches to the parent metal.

On the contrary, when the figure 40 was examined, crack growth seemed to have high rate through the weld and the HAZ compared to parent metal. However, the data taken from the parent metal was not enough to predict a pattern. GMAW did not revealed distinguished change in crack growth rate and it seemed to have a slower growth compared to HPAW. Nevertheless, when the crack growth rate data was analyzed, HPAW reached a maximum

growth rate of $1.8*10^{-4}$ (mm/cycle), where the maximum growth rate of GMAW was $2.3*10^{-4}$(mm/cycle). For both figure 39 and 40 the weld zone and the HAZ were separated for ease of understanding. Red areas represent the weld zone whereas green areas represent the HAZ and the rest belong to the parent metal.

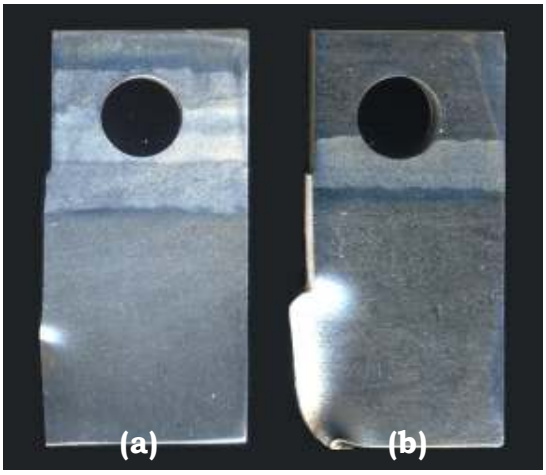

Figure 38: CT specimens in T-L_L orientation (a) GMAW and, (b) HPAW.

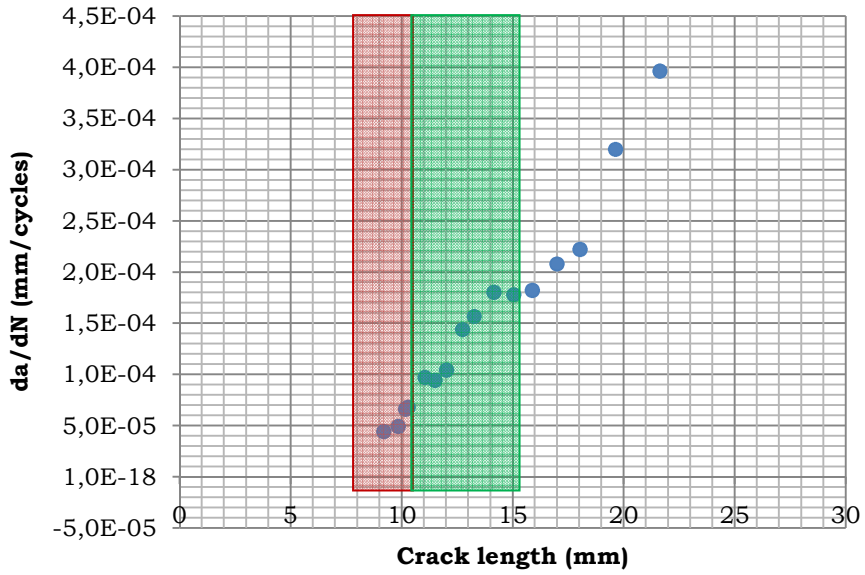

Figure 39: Crack growth rate vs. crack length-HPAW, showing the crack growth rate in weld (red) and heat affected (green) zones.

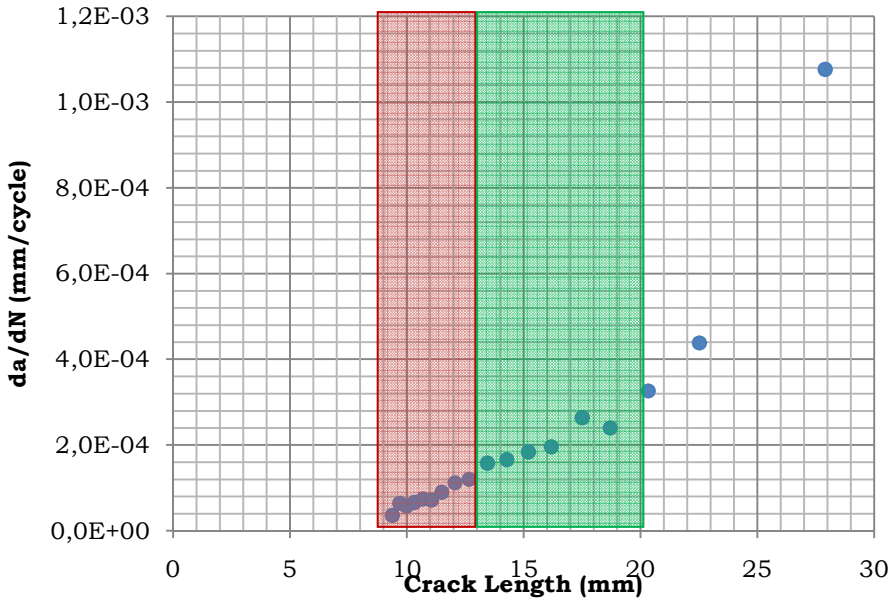

Figure 40: Crack growth rate vs. crack length – GMAW, showing the crack growth rate in weld (red) and heat affected (green) zones.

CHAPTER 5

CONCLUSION

In the presented study, a new welding technique (HPAW) was investigated by using a duplex stainless steel as the material to be welded, and compared with a conventional technique (GMAW) by metallurgical and mechanical examinations. The following conclusions can be drawn from this study:

1. HPAW resulted in deeper penetration compared to GMAW, where HPAW welded in 1 pass and GMAW welded in 4 passes for the same plate thickness.
2. Overall heat input of HPAW was low compared to that of GMAW, resulting in less residual stresses, thinner HAZ and fine grain structure.
3. Phase balance was deteriorated in fusion zone for both welding techniques. Secondary γ formation in acicular form was observed in the fill passes of GMAW subjected to heat treatment by cap passes. On the other hand, high ferrite formation was observed especially in the root of HPAW where welding was autogeneous.
4. Hardness profiles were very useful to predict the HAZ widths for both welding techniques. Furthermore, the overall hardness of HAZ of GMAW was higher than that of HPAW. That may be pointed out the intermetallic phases present in the HAZ of GMAW, which are not preferred.
5. Charpy impact toughness results showed that the overall toughness of HPAW was higher than that of GMAW. Combined with the harness examinations, HPAW showed closer results to the parent metal. This

can be explained that the weld zone and especially the HAZ of HPAW were very thin compared to that of GMAW. Therefore, especially for the toughness examinations the results were coming from both HPAW and the parent metal.

6. Fatigue crack growth examinations can be examined in two ways. For the orientation where the crack propagates along the weld metal; HPAW showed high crack growth rate and brittle fracture surfaces due to the high ferrite content. However, in the case where the crack propagation was perpendicular to the welding direction; HPAW resulted in analogous crack growth rate with the parent metal. This phenomenon can be explained again the thinner weld zone and HAZ obtained by the HPAW and the results contain data mostly from the parent metal.

HPAW revealed almost similar, at some points better, metallurgical and mechanical properties compared to GMAW. Furthermore, HPAW is more advantageous in practical application and economical by means of low number of passes, and heat input. However, the autogenous welding zone should be prevented to preserve the superior mechanical properties arising from the phase balance of austenite and ferrite.

REFERENCES

1. JO., Nilsson; Super duplex stainless steels. *Materials Science and Technology.* 1992, Vol. 8, pp. 685-700.

2. JD., Kordatos, G., Fourlaris & G., Papadimitriou; The effect of cooling rate on the mechanical and corrosion properties of SAF 2205 (UNS 31803) duplex stainless steel welds. *Scripta Metallurgica.* 2001, Vol. 44, pp. 401 – 408.

3. A., Westin. & EM., Fellman; Effect of laser and laser hybrid welding on the corrosion performance of a lean duplex stainless steel. *Journal of Laser Applications.* 2010, Vol. 22, pp. 150 – 159.

4. JO., Nilsson, P., Kangas, T., Karlsson and A., Wilson; Mechanical properties, microstructural stability and kinetics of σ phase formation in 29Cr-6Ni-2Mo-0,38N super duplex stainless steel. *Metallurgical and Materials Transactions A.* 2000, Vol. 31A, pp. 35 – 40.

5. T., Omura, T., Kushida & Y., Komizo; Microstructural features and corrosion properties in laser welded duplex stainless steels. *Welding International.* 2000, Vol. 14, pp. 257 – 260.

6. NA., McPherson, H., Samson, TN., Baker & SN., Fernandez; Steel microstructures in autogenous laser welds. *Journal of Laser Applications.* 2000, Vol. 15, pp. 200-211.

7. JS., Ku, NJ., Ho & SC., Tjong; Properties of electron beam welded SAF 2205 duplex stainless steel. *Journal of Materials Processing Technology.* 1997, Vol. 63, pp. 770-775.

8. J.C., Ion; Laser Processing of Engineering Materials; Keyhole welding. . Burlington : Elsevier Butterworth-Heinemann, 2005, pp. 395 – 455.

9. S., Henrik; Fracture toughness properties of duplex stainless steels. *Doctoral Thesis.* Stockholm, Sweden : Department of Materials Science and Engineering, Royal Institute of Technology, 2006.

10. N.I.A., Haddad; The development of microstructure in duplex stainless steel welds. *PhD Thesis.* Cambridge : Pembroke College, 1989.

11. TH.,Chen, KL.,Weng, JR., Yang; The effect of high temperature exposure on the microstructural stability and toughness property in a 2205 duplex stainless steel. *Mater Sci Eng A.* A338, 2002, Vol. 259, 70.

12. W., Zhang, T., Debroy, TA., Palmer, JW., Elmer; Modelling of δ-ferrite formation in a duplex stainless steel weld, considering non-uniform starting microstructure. *Acta Materiala.* 53, 2005, Vol. 4441, 53.

13. CH., Sump, and GC., Bodine; Duplex Stainless Steel. [ed.] R. A. Lula. s.l. : *American Society for Metals*, 1983.

14. S., McKenzie, HM., Flower, and DRF., West; *Conf. Proc. Stainless Steels.* 1984.

15. J., Michalska, M., Sozanska; Qualitative and quantitative analysis of σ and x phases in 2205 duplex stainless steels. *Material Characterization.* 2006, Vol. 56, p. 355.

16. S., Topolska, J., Łabanowski; Effect of microstructure on impact toughness of duplex and superduplex stainless steels. vol. 36, 2 : J*ournal of achievements in materials and manufacturing engineering,* 2009. 142.

17. O., Smuk, P., Nenonen, H., Hanninen and J., Liimatainen; Precipitation of Secondary Phases In Duplok 27 Duplex Stainless Steel With Emphasis on Copper Effects, Helsinki University of Technology, 2002. p. 72. *Internal Report TKK-MTR 6/02.*

18. Practical guidelines for the fabrication duplex stainless steels. *International Molybdenum Association.* 2001. p. 9.

19. *Standard Specification for Chromium and Chromium-Nickel Stainless Steel Plate, Sheet, and Strip for Pressure Vessels and for General Applications.* ASTM A240/A240M-11a.

20. T., Thorvaldsson, H., Eriksson, J., Kutka, A., Salwén; Influence of microstructure on mechanical properties of a duplex stainless steel. Göteborg, Sweden : 1984. Stainless Steel. pp. 101-105.

21. F., Iacoviello, M., Boniardi, GM., La Vecchia; Fatigue crack propagation in austeno-ferritic duplex stainless steel 22Cr5Ni. *Internatioanl Journal of Fatigue.* 1999, 21, pp. 957-963.

22. J.-B., Vogt. Fatigue properties of high nitrogen steels. *Mater. Proc. Tech.* 117, 2001, pp. 364-369.

23. *Stainless steels. Technical delivery conditions for sheet/plate and strip of corrosion resisting steels for general purposes.* BS EN10088-2:2005.

24. *Seamless steel tubes for pressure purposes. Technical delivery conditions. Stainless steel tubes.* BS EN10216-5:2004.

25. *Standard Specification for Seamless and Welded Ferritic/Austenitic Stainless Steel Tubing for General Service.* ASTM A789 / A789M - 10a.

26. *Standard Specification for Seamless and Welded Ferritic/Austenitic Stainless Steel Pipe.* ASTM A790 / A790M - 11.

27. *Standard Specification for Forged or Rolled Alloy and Stainless Steel Pipe Flanges, Forged Fittings, and Valves and Parts for High-Temperature Service.* ASTM A182 / A182M - 11a.

28. *The Pressure Equipment Directive (97/23/EC)*: European Parliament and the European Council.

29. *Unfired pressure vessels - Part 3: Design.* EN 13445-3.

30. *Boiler and Pressure Vessel Code Section VIII.* ASME.

31. B., Stig; On the effect of plate thickness in fatigue of welds. *Engineering Fracture Mechanics.* 1985, Vol. 21, 2, pp. 423-435.

32. C., Capela, J.D., Costa, F., Antunes, J.M., Ferreira; Thermal fatigue assessment of components made with particulate polymer composites. *Theoretical and Applied Fracture Mechanics.* 2004, 42, pp. 171-181.

33. CM., Pang, JH., Song; Crack growth and closure behavior of short fatigue crack. . *Engineering Fracture Mechanics .* 1994, 47, p. 327.

34. H., Sieurin, R., Sandström; Austenite reformation in the heat affected zone of duplex stainless steel 2205. *Material Science Engineering A.* 2006, 418, pp. 250-256.

35. T., Süha, Y., Koray and B., Caner; *Microstructural characterization of heat affected zone in the 2507 SDSS welds.* Ankara, 2008.

36. J.R., Davis; Corrosion of weldments. *Materials Park,* ASM International, 2006. OH 44073-002.

37. M., Barry, O., Vasile, W., Andrew; Duplex stainless steel welding: best practices. *Stainless Steel World.* 2007, pp. 53-63.

38. R. Badji, B.Belkessa, H. Maza, M.Bouabdallah, B.Bacroix, C.Kahloun. Effect of Post Weld Heat Treatment on Microstructure and Mechanical Properties of Welded 2205 Duplex Stainless Steel. *Materials Science Forum.* 2004, Vols. 467-470, pp. 217-222.

39. I., Dykhno, R., Davis; Joining GMAW and GTAW. *The Fabricator.* 2006, pp. 60 – 62.

40. T., Sándor, J., Dobránszky; Experiences of ATIG welding of austenitic stainless steel plates .

41. Steel and iron - Sampling and preparation of samples for the determination of chemical composition. *ISO 14284:1996.*

42. Charpy Impact Test on Metallic Materials. *TS EN 10045-1 .*

43. P., Paris, and F., Erdogan; A Critical Analysis of Crack Propagation Law. *Journal of Basic Engineering.* 1963, Vol. 85, pp. 528-534.

44. N., Ki-Woo, et al. Fatigue Crack Propagation of Super Duplex Stainless Steel with Dispersed Structure and Time-Frequency Analysis of Acoustic Emission. *METALS AND MATERIALS International.* 2001, Vol. 7, 3, pp. 227-231.